

Cantharidin-Loaded Biomimetic MOF Nanoparticles Cascade To Enhance Fenton Reaction Based On Amplified Photothermal Therapy

Xiao Cheng

Dalian University of Technology

Ye Liu

Dalian University of Technology

Hao Zhou

Dalian University of Technology

Junke Leng

Dalian University of Technology

Xiaofeng Dai

Dalian University of Technology

Dong Wang

Panjin People's Hospital

Kun Ma

Dalian University of Technology

Changhao Cui

Dalian University of Technology

Jijun Fu

Guangzhou Medical University

Zhaoming Guo (✉ guozm@dlut.edu.cn)

Dalian University of Technology <https://orcid.org/0000-0003-1295-6838>

Research

Keywords: Metal organic framework (MOF), Tumour microenvironment (TME), Fenton reaction, Photothermal therapy (PTT), Heat shock response (HSR)

Posted Date: June 8th, 2021

DOI: <https://doi.org/10.21203/rs.3.rs-575033/v1>

License:   This work is licensed under a Creative Commons Attribution 4.0 International License.

[Read Full License](#)

Version of Record: A version of this preprint was published at Biomaterials Science on January 1st, 2021.
See the published version at <https://doi.org/10.1039/D1BM01396C>.

1 Cantharidin-Loaded Biomimetic MOF
2 Nanoparticles Cascade to Enhance Fenton
3 Reaction Based on Amplified Photothermal
4 Therapy

5 Xiao Cheng ^a, Ye Liu ^a, Hao Zhou ^b, Junke Leng ^a, Xiaofeng Dai ^a, Dong Wang ^c, Kun
6 Ma ^a, Changhao Cui ^a, Jijun Fu ^{*,d}, Zhaoming Guo ^{*,a},

7 ^a School of Life and Pharmaceutical Sciences, Dalian University of Technology, Panjin,
8 Liaoning 124221, China

9 ^b School of Food and Environment, Dalian University of Technology, Panjin, Liaoning
10 124221, China

11 ^c Panjin People's Hospital, Panjin, Liaoning 124221, China

12 ^d The Key Laboratory of Molecular Target & Clinical Pharmacology, The First
13 Affiliated Hospital of Guangzhou Medical University, Guangzhou Medical University,
14 Guangzhou, 511436, China

15 * **Corresponding author:**

16 School of Life and Pharmaceutical Sciences, Dalian University of Technology, Panjin,
17 Liaoning 124221, China.

18 Tel: +86-427-2631427. Fax: +86-427-2631889. E-mail address: guozm@dlut.edu.cn

19 (Zhaoming Guo)

20 The Key Laboratory of Molecular Target & Clinical Pharmacology, The First Affiliated
21 Hospital of Guangzhou Medical University, Guangzhou Medical University,
22 Guangzhou, 511436, China

23 E-mail address: fujj@gzhmu.edu.cn (Jijun Fu)

24
25 Key Words: Metal organic framework (MOF); Tumour microenvironment (TME);
26 Fenton reaction; Photothermal therapy (PTT); Heat shock response (HSR)

27 ABSTRACT

28 The treatment efficiency of Fenton reaction is expected to be greatly restricted due to
29 problems such as inefficient delivery of Fenton catalysis, limited H₂O₂ concentration
30 and uneven tumour tissue. Accurate photothermal therapy (PTT) can to some extent
31 improve the efficiency of Fenton catalysis by raising temperature. However, the heat
32 shock response (HSR) of tumour cells caused by PTT and Fenton reaction can attenuate
33 the treatment effect. In this study, we developed a combined treatment platform based
34 on the Fenton reaction mediated by iron ions consisting of a metal organic framework,
35 i.e., PPy-CTD@MIL-100@MPCM nanoparticles (PCMM NPs), and we explored the
36 inhibitory effect of PCMM NPs on the heat shock response (HSR). PCMM NPs can be
37 recruited into tumour tissues through the response of biomacromolecules on the surface
38 of macrophage cell membranes (MPCMs) to tumour cell signaling molecules, thereby
39 increasing retention and accumulation. The photothermal effect of polypyrrole (PPy)
40 can stimulate the HSR of tumour, and loaded HSP inhibitor-canharidin (CTD) can

41 inhibit this response to a large extent. In addition, the heat generated during the PTT
42 process can accelerate the release of iron ions from the PCMM NPs and simultaneously
43 improve the efficiency of the Fenton reaction to achieve a combined treatment of
44 tumour PTT, Fenton therapy and chemotherapy.

45 **1. Introduction**

46 The tumour microenvironment (TME) closely related to tumours is an extremely
47 complex integrated system that is composed of various stromal cells and extracellular
48 matrix(1). TME with the characteristics of hypoxic, higher levels of glutathione (GSH)
49 and reactive oxygen species (ROS)(2) provides a suitable environment for tumour
50 development. On the other hand, these features furnish an opportunity for some therapy
51 methods to improve anti-tumour capabilities.

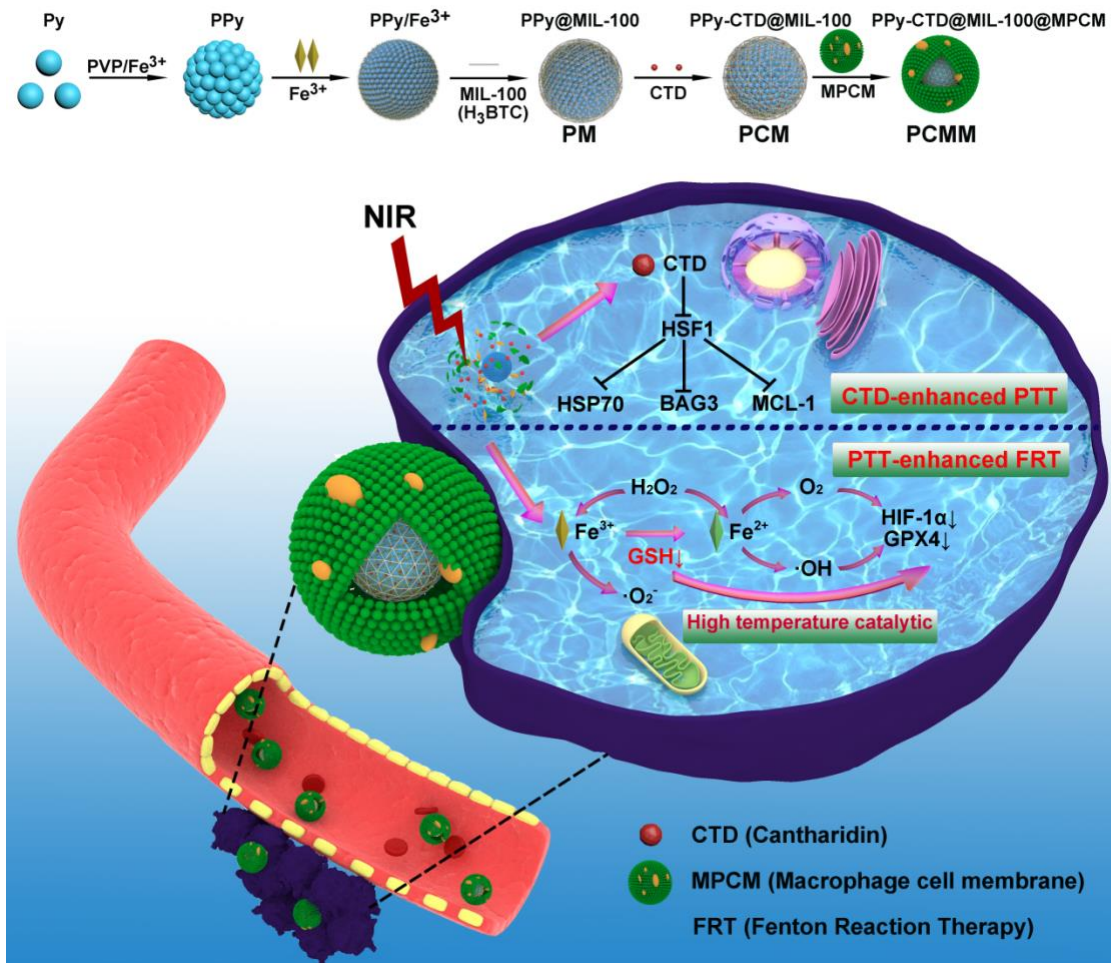
52 Recently, studies have shown that the TME provides an excellent stage for Fenton
53 therapy, a therapeutic strategy mediated by iron ions(3, 4). The Fenton reaction can
54 consume excessive H₂O₂ in tumour tissue, generate the strongest ROS, i.e., hydroxyl
55 radicals(5, 6), to kill tumour cells and simultaneously generate oxygen to improve the
56 hypoxic state of the TME(7). These characteristics are absolutely helpful for inhibiting
57 tumour proliferation and angiogenesis(8). However, Fenton reaction is often inefficient
58 due to the limited H₂O₂ concentration, uneven tumour tissue and other conditions (9,
59 10). Therefore, the Fenton reaction alone is not sufficient to achieve the desired
60 therapeutic effect, and combination therapy is necessary. According to the classic
61 thermodynamic molecular collision theory, increasing the temperature may be a

62 feasible way to improve the efficiency of the Fenton reaction(9, 11). Therefore, accurate
63 and effective PTT can be a good partner(12).

64 The MOF is an excellent platform for combination tumour therapy. Organic
65 polypyrrole (PPy) has the advantages of high photothermal conversion efficiency and
66 good biocompatibility, so we chose it as the central photothermal agent in the MOF
67 (13). Loading Fe^{3+} as the skeleton of the MOF can achieve the Fenton reaction and
68 consume GSH to downregulate glutathione peroxidase 4 (GPX4) to mediate tumour
69 cell ferroptosis(14).

70 However, damaging treatments such as PTT or Fenton therapy can cause the HSR,
71 which is a general protection mechanism for tumour cells to resist external damage(15,
72 16). This is the key to successfully eradicating tumour that effectively inhibiting tumour
73 HSR in damaging treatments(17). As a therapeutic drug used for treating liver cancer
74 and melanoma, cantharidin (CTD) has been identified in past studies as an inhibitor of
75 heat shock transcription factor 1 (HSF1) and has a good effect on inhibiting the
76 HSR(18). Therefore, we used CTD as a model drug to resist HSR and improve the
77 therapeutic effect. Finally, to improve the targeting and long circulation of
78 nanoparticles, we coated macrophage cell membranes (MPCMs) around the
79 nanoparticles, whose surface biomacromolecules can actively recruit to tumour tissues
80 and increase retention and accumulation because of their ability to recognize tumour
81 cells and respond to tumour region signal molecules.(19-21).

82 Considering the interrelationship between the TME and tumour therapy, we proposed
83 a treatment strategy with a MOF as the framework, PPy as the core, CTD as the model
84 drug, loading with a large amount of Fe^{3+} , and MPCM as the outer coating. This strategy
85 has the following behaviours: 1) MPCM can give active targeting to nanoparticles(22,
86 23), and escape the immune clearance of macrophages to obtain long-lasting
87 circulation(24). 2) After reaching the tumour, a laser can be used to irradiate the tumour.
88 At this time, the photothermal agent reacts. Under the catalysis of heat, the coated
89 MPCM ruptures and the PCM releases CTD and iron ions. 3) CTD is used for tumour
90 treatment as a chemotherapeutic agent and inhibition of the HSR in tumour cells. 4) In
91 GSH overexpressed tumour tissues, Fe^{3+} is reduced to Fe^{2+} , which mediates the down-
92 regulation of GPX4 and leads to ferroptosis(25). 5) Under high temperature, Fe^{2+}
93 undergoes a strong Fenton reaction with H_2O_2 in the TME to generate hydroxyl free
94 radicals that kill tumour cells. Fe^{2+} can also generate oxygen to improve the anoxic
95 TME(26, 27), downregulate HIF-1 α and inhibit tumour expansion. This strategy
96 worked well in both cellular and mouse models, indicating that it is a very effective
97 tumour treatment strategy.



99 **Scheme 1.** Schematic illustration of the preparation of PCMM NPs and cantharidin-
 100 loaded biomimetic MOF nanoparticles cascade to enhance Fenton reaction based on
 101 amplified photothermal therapy.

102 2. Materials and methods

103 2.1. Materials

104 Polyvinylpyrrolidone (PVP, K30, MW \approx 45000-58000), pyrrole (Py), FeCl₃·6H₂O
 105 (97%), CTD, 1,3,5-Benzenetricarboxylic acid (H₃BTC), doxorubicin hydrochloride
 106 (DOX), DMPO (5,5-dimethyl-1-pyrroline N-oxide), Rhd B (Rhodamine B) and Phe
 107 (1,10-phenanthroline monohydrate) were obtained from Aladdin (Shanghai, China).

108 Phenylmethylsulfonyl fluoride (PMSF) was obtained from Macklin (Shanghai, China).
109 4',6-Diamidino-2-phenylindole (DAPI) was obtained from Solarbio (Beijing, China).
110 A Calcein-AM/PI Double Stain Kit was provided by Yeasen (Shanghai, China). An
111 Annexin V-FITC/PI Cell Apoptosis Kit, DCFH-DA and a Cell Counting Kit-8 (CCK-
112 8) were purchased from APE×BIO. Foetal bovine serum (FBS), RPMI-1640 Medium
113 Modified, Dulbecco's Modified Eagle's Medium (DMEM), trypsin-EDTA and
114 penicillin-streptomycin were obtained from HyClone. RIPA lysis buffer and BCA
115 assay kits were purchased from Solarbio (Beijing, China). Protease inhibitor cocktail
116 (EDTA-Free, 100x in DMSO) was purchased from APE×BIO. All antibodies were
117 obtained from Abcam.

118 **2.2. Preparation of PCMM**

119 **2.2.1. Synthesis of PM (PPy@MIL-100)**

120 The process of PM synthesis has improved from previously reports(28, 29). 1 g of PVP
121 was completely dissolved in 25 mL of deionized water and stirred for 30 min, and 2
122 mM of pyrrole was added to the PVP solution and stirred for 10 min. Next, 3 mM (1
123 mL) FeCl₃·6H₂O solution was added to the mixed solution, and stirring was continued
124 for 4 h. A volume of 600 μL of PPy NPs was placed into 10 mL of ethanol solution and
125 stirred in a water bath at 75 °C. Subsequently, 1 mM (1 mL) of H₃BTC solution was
126 added to the mixed solution, and stirring was continued for 30 min to obtain a
127 framework structure before washing several times with deionized water to remove
128 excess ions and obtain PM.

129 **2.2.2. Preparation of PCM (PPy-CTD@MIL-100)**

130 CTD 100 $\mu\text{L}/\text{mL}$ was prepared. PM (1 g/mL) was dissolved in 1 mL of ethanol, and 1
131 mL of 100 $\mu\text{L}/\text{mL}$ CTD was added and stirred for 24 h. PCM was obtained by
132 centrifugation, and 100 μL of supernatant was collected. The absorbance value at 228
133 nm was detected, and the drug loading was determined.

134 **2.2.3. Preparation of MPCM**

135 MPCM was extracted according to previous reports(24). After medium removal and
136 two washes with PBS, RAW264.7 cells were collected in a centrifuge tube. 10 mL of
137 NaHCO_3 (1 mmol/L), 0.05% Trypsin-EDTA (0.2 mmol/L) and PMSF (1 mmol/L) were
138 added overnight. After crushing 10 times, the pellet was centrifuged at 3200 g for 5 min,
139 and the supernatant was centrifuged at 1×10^5 g for 30 min. PBS was added for
140 resuspension.

141 **2.2.4. Preparation of PCMM (PPy-CTD@MIL-100@MPCM)**

142 The equal volume of 2 mg/mL MPCM and PCM were mixed, and the above mixed
143 solution was extruded through 200 nm polycarbonate membrane by a micro extruder
144 for no less than 11 times. Finally, PCMM NPs was obtained.

145 **2.3. Characterization**

146 Transmission electron microscopy (TEM) (FEI Tecnai G2 F30) was used to
147 characterize the morphology of the nanoparticles. Dynamic light scattering (DLS)
148 analysis using a Malvern Zeta sizer Nano ZS (Malvern, UK) was conducted to measure

149 the hydrated particle size of Py, PM and PCMM. A UV-Vis spectrophotometer
150 (Thermo Scientific Instrument Co., Ltd.) was used to measure the optical absorbance.
151 An electronic paramagnetic resonance apparatus (Bruker, Germany) was used to
152 identify the types of ROS. An NIR laser with a centre wavelength of 808 nm was used
153 for irradiation (Changchun New Industries Optoelectronics Tech. Co., Ltd.). A
154 PerkinElmer in vivo imager was used to record the drug distribution in vivo.

155 **2.4 The ability of PCM to generate ROS and the ability to reduce GSH**

156 In order to ignore the influence of macrophage membrane on the reaction, we observed
157 the changes at 650 nm to evaluate the amount of $\cdot\text{OH}$ produced by the Fenton reaction
158 between TMB and PCM at different temperatures (25 °C and 47 °C). Additionally,
159 more accurate DMPO was used as a capture agent, and electron paramagnetic resonance
160 was used to determine the type of ROS generated. A reducing GSH Kit and Phe were
161 used to measure the ability of PCM to reduce GSH at different temperatures (25 °C and
162 47 °C). The change in absorbance at 425 nm was used to monitor PCMM NPs (75
163 $\mu\text{g/mL}$) containing H_2O_2 in the presence/absence of GSH (1 mM). By detecting the
164 change in absorbance at 525 nm, the GSH consumption capacity of Fe^{3+} in PCMM NPs
165 (0.2 mM Phe, 75 $\mu\text{g/mL}$ PCMM NPs) containing H_2O_2 was observed in the presence
166 or absence of 10 mM GSH.

167 **2.5 PCMM thermal performance**

168 To further study the photothermal performance of PCMM NPs, we explored the
169 photothermal performance of different light intensities (500, 750 and 1000 mW/cm^2)

170 and different drug concentrations (0, 25, 50 and 75 $\mu\text{g/mL}$, using DMEM complete
171 medium to prepare different concentrations). The photothermal effect was studied
172 under a simulated human body temperature environment (37 $^{\circ}\text{C}$). One millilitre of
173 PCMM NPs at different concentrations was placed in a 37 $^{\circ}\text{C}$ environment, 808 nm
174 near-infrared lasers with different light intensities provided irradiation for 10 min, and
175 the temperature was recorded every 30 s using a digital thermocouple device. To
176 observe the thermal performance of PCMM NPs more intuitively, an infrared thermal
177 imager (FLIR, USA) was used to capture infrared thermal images of the suspension of
178 PCMM NPs every 2 min. To calculate the photothermal conversion efficiency (η) of
179 PCMM NPs, a suspension of PCMM NPs (75 $\mu\text{g/mL}$, 1.0 mL) and deionized water (1.0
180 mL) was treated with an NIR laser (1 W/cm^2) for 20 min. After the laser was turned off,
181 the suspension was naturally cooled to ambient temperature. The temperature of the
182 solution was measured every 30 s, and a temperature graph was drawn. To an amount
183 of 75 $\mu\text{g/mL}$ of PCMM NPs at 37 $^{\circ}\text{C}$, 1000 mW/cm^2 was applied with a 808 nm near-
184 infrared laser for 10 min, and after the laser was turned off, the solution was cooled to
185 37 $^{\circ}\text{C}$. This process was repeated five times. The light resistance of the nanoparticles
186 was tested by recording the temperature of the solution. To measure the photothermal
187 conversion efficiency, PCMM NPs (75 $\mu\text{g/mL}$, 1.0 mL) and deionized water (1.0 mL)
188 were irradiated with a NIR laser (1 W/cm^2) for 20 min. After the laser was turned off,
189 the suspension was naturally cooled to ambient temperature. The temperature of the
190 solution was measured every 30 s, and a temperature graph was drawn.

191 **2.6 In vitro drug release**

192 A dialysis method was used to study the release behaviour of CTD in PCMM NPs after
193 0,500, 750 and 1000 mW/cm² laser irradiation. In short, PCMM NPs (1 mg/mL) were
194 dissolved in 1 mL of PBS (pH 7.4), and the mixture was placed in a dialysis bag (MW
195 = 14000). The dialysis bag was placed in PBS buffer (70 mL) and shaken horizontally
196 (80 rpm) in a shaker at 37 °C to release the medium. At predetermined time points (0,
197 2, 4, 6, 8, 12, 24 and 48 h), 100 µL of the solution was removed from the buffer medium,
198 and the amount of CTD released was measured using a UV-Vis spectrophotometer.

199 **2.7 Cell culture**

200 All cell lines used in this study were purchased from Procell Biotech (Wuhan, China).
201 Human liver cancer cells (HepG2), mouse mononuclear macrophage leukaemia cells
202 (RAW 264.7), human embryonic kidney cells (293T) and mouse liver cancer cells
203 (HepA1-6) were maintained in 10% FBS, 100 µg/mL penicillin and 100 mg/mL
204 streptomycin in complete DMEM. Mouse liver cancer cells (H22) were cultured in
205 complete 1640 medium. All of the above cell lines were cultured at 37 °C in a humid
206 environment containing 5% CO₂.

207 **2.8 In vitro safety analysis**

208 Blood from BALB/c mice was used to analyse the biocompatibility of PM, PCM and
209 PCMM. Whole blood was collected from mice via retro-orbital bleeding, and then it
210 was added to an EDTA anticoagulation tube and shaken evenly. The blood was

211 centrifuged at 1500 rpm at 4 °C for 5 min and washed 3 times with PBS. An amount of
212 20 µL of red blood cell suspension was added to various concentrations of PM, PCM
213 and PCMM in PBS suspension (25, 50 and 75 µg/mL; 1.0 mL). After shaking at 37 °C
214 for 4 h in a shaker at a speed of 100 r/min, images were captured. Finally, 100 µL of
215 supernatant was removed from each experimental group, and the absorbance was
216 measured at 540 nm using a microplate reader. Deionized water and PBS (pH 7.4) were
217 used as positive and negative controls, respectively. The haemolysis rate was calculated
218 using the following formula:

$$219 \quad Haemolysis(\%) = (A_{Sample} - A_{Negative}) / (A_{Positive} - A_{Negative}) \times 100\%$$

220 The viability of cells in PM, PCM and PCMM at different drug concentrations (0, 25,
221 50 and 75 µg/mL) was tested using a CCK-8. HepG2 and 293T cells (5×10^4 /100 µL)
222 were seeded in 96-well plates and incubated overnight to allow them to attach to the
223 bottom. Different concentrations of PM, PCM, and PCMM were incubated with HepG2
224 and 293T cells for 48 h. An amount of 10 µL CCK-8 was added to each well, and the
225 absorbance at 450 nm was detected.

226 **2.9 Cellular uptake assay**

227 The uptake of PM, PCM, and PCMM by a variety of cells (RAW264.7, 293T, HepG2
228 and HepA1-6) was evaluated by CLSM and flow cytometry. The autofluorescence of
229 DOX (adriamycin) was used instead of CTD to detect the uptake ability, so we prepared
230 PDM (PPy-DOX@MIL-100) and PDMM (PPy-DOX@MIL-100@MPCM). To
231 directly observe the uptake capacity, four types of cells (1×10^4 , 500 µL) were cultured
232 on round slides and incubated with medium containing PDM and PDMM. After the

233 proper incubation time, the round glass slides were washed with PBS 3 times and fixed
234 with 4% paraformaldehyde for 15 min. The nucleus were stained with DAPI (5 $\mu\text{g}/\text{mL}$)
235 for 15 min and washed twice with PBS. Finally, the cells were imaged by CLSM. To
236 determine the cell uptake ratio, RAW264.7, 293T, HepG2 and HepA1-6 cells were
237 inoculated in 24-well plates and cultured overnight. The cells were incubated with 50
238 $\mu\text{g}/\text{mL}$ PDM and PDMM (15 $\mu\text{g}/\text{mL}$ DOX) at 37 $^{\circ}\text{C}$ for 2 h, and the samples were
239 collected and analysed by flow cytometry.

240 **2.10 Generation and determination of ROS**

241 A DCFH-DA reactive oxygen analysis kit was used to evaluate the ROS generation
242 ability of the nanoparticles. HepG2 cells were seeded in 24-well plates (5×10^5 cells/well)
243 and incubated overnight. On the next day, the medium was removed, PCMM (0, 25, 50
244 and 75 $\mu\text{g}/\text{mL}$) containing H_2O_2 was added to the medium, and laser (808 nm; 0, 500,
245 750 and 1000 mW/cm^2 ; 10 min) treatment was applied. The cells were washed and
246 treated with serum-free medium containing DCFH-DA (10 μM) for 20 min.
247 Subsequently, the cells were again washed 3 times with serum-free medium. Finally,
248 the generation of ROS was observed using confocal laser scanning microscopy (CLSM,
249 Heidelberg, Germany).

250 **2.11 In vitro cytotoxicity of single PTT and combination therapy**

251 The effects of single PTT and combination therapy were evaluated by AM-PI double
252 staining experiments, flow cytometry and CCK-8 assays. For qualitative analysis,
253 HepG2 cells were seeded in 96-well plates overnight. Under the premise of controlling

254 a single variable, PCMM (0, 25, 50 and 75 $\mu\text{g}/\text{mL}$) was added and incubated for 6 h in
255 the presence or absence of H_2O_2 . After treatment with a NIR laser (808 nm, 0, 500, 750
256 and 1000 mW/cm^2 ; 10 min), the cells were placed in an incubator and incubated for 4
257 h. Live cells and dead cells were stained with calcein-acetoxymethyl ester (calcein-AM)
258 and propidium iodide (PI), and fluorescent images were captured with an inverted
259 fluorescence microscope (Leica DMI4000B) for qualitative analysis. The quantitative
260 cytotoxicity results were obtained using flow cytometry. Similar to CLSM, after
261 staining of live and dead cells with Annexin V FITC and PI, respectively, quantitative
262 analysis was performed by flow cytometry. After treatment with the same treatment
263 conditions again, 10 μL of CCK-8 was added to each well and incubated for another 1
264 h at 37 $^\circ\text{C}$. Finally, a microplate reader (BioTek, USA) was used to measure the
265 absorbance of each well at 450 nm to quantify the cytotoxicity of PCMM.

266 **2.12 Exploration of the inhibitory effect of PCMM NPs on HSR**

267 To explore the inhibitory effect of PCMM NPs on the HSR under a single photothermal
268 treatment, we conducted western blotting. HepG2 cells were incubated with PCMM
269 NPs of different concentrations (0, 25, 50 and 75 $\mu\text{g}/\text{mL}$) for 6 h, irradiated at 37 $^\circ\text{C}$
270 with a NIR laser with different light intensities (808 nm; 0, 500, 750 and 1000 mW/cm^2 ;
271 10 min), the protein was extracted after 12 h of incubation. HSF1 downstream target
272 proteins (HSP70, BAG3 (Bcl-2 associated oncogene domain 3) and MCL-1) were used
273 to evaluate the expression levels of heat shock proteins (HSPs).

274 **2.13 Animal model**

275 Based on the above experimental results, we screened the optimal conditions for in vivo
276 experiments. A tumour-bearing animal model was established for female BALB/c mice
277 (6 weeks old, Liaoning Changsheng Biotechnology Co., Ltd.). H22 cells (1×10^6 ,
278 suspended in 100 μ L PBS) were injected subcutaneously into the right armpit of each
279 mouse, and the tumour volume was measured one week later. When the tumour size
280 reached 50 mm³, the mice were further used for in vivo experiments. All animal
281 procedures in this investigation were approved by the Institutional Animal Care and
282 Use Committee of Dalian University of Technology.

283 The tumour volume is defined as $V = W^2L/2$, where W and L represent the shorter and
284 longer diameters of the tumour, respectively.

285 **2.14 Drug distribution in the body**

286 PCMM-Rhd B and PCM-Rhd B were prepared. PCMM and PCM were mixed with Rhd
287 B in equal proportions and centrifuged to obtain PCMM-Rhd B and PCM-Rhd B.
288 PCMM-Rhd B and PCM-Rhd B were injected into shaved BALB/c mice with tumours
289 up to 1000 mm³. A PerkinElmer in vivo imager was used to record the drug distribution
290 in vivo at 0 h, 0.5 h, 2 h, 6 h, 12 h, 24 h, 48 h and 72 h.

291 **2.15 In vivo drug efficacy evaluation**

292 The tumour-bearing mice were randomly divided into eight groups (n = 4): (1) PBS, (2)
293 PBS+1000 mW/cm², (3) PMM, (4) PMM+1000 mW/cm², (5) PCMM, (6) PCMM+500
294 mW/cm², (7) PCMM+750 mW/cm² and (8) PCMM+1000 mW/cm². Each group of
295 mice was injected intravenously with 5 mg/kg PBS, PMM or PCMM (0.1 mg/kg CTD,

296 100 μ L). For groups (2), (4), (6), (7) and (8), the tumour area of the mice was irradiated
297 with an NIR laser (808 nm, 10 min) 12 h after administration. Every two days after
298 treatment, the tumour size and weight of each mouse were measured with digital
299 calipers and an electronic balance. After 15 days of treatment, blood was collected from
300 all mice for routine blood analysis. Finally, the mice were sacrificed and dissected. The
301 tumour was removed, weighed and photographed. The main organs (heart, liver, spleen,
302 lung, kidney) and tumour of the mice were fixed in 10% formalin. 5 μ m paraffin
303 sections were prepared. After deparaffinization in xylene and dehydration in a graded
304 series of alcohols, haematoxylin and eosin (H&E) was used to stain the organ-loaded
305 slides. The nucleus was stained blue, and the cytoplasm was stained red. The cells were
306 observed using an optical microscope.

307 **2.16 Immunofluorescence**

308 To study the therapeutic mechanism of PCMM NPs, we performed
309 immunofluorescence staining on tumour tissue sections. The treated mice were
310 sacrificed, and tumour sections were taken and fixed for staining. To assess the activity
311 of GPX4, anti-rabbit GPX4 and Alexa Fluor 488® secondary antibodies were used for
312 immunofluorescence staining. Anti-mouse HIF-1 α and Alexa Fluor 594® secondary
313 antibodies were used to evaluate the expression of HIF-1 α .

314 **2.17 Statistical analysis**

315 All experiments were repeated at least 3 times, and all results are expressed as the
316 mean \pm SD. A two-tailed heteroscedasticity Student's t-test was used to evaluate
317 statistical significance (*, P <0.05; **, P <0.01; and ***, P <0.001).

318 **3. Results and discussion**

319 **3.1 Preparation and characterization of PCMM**

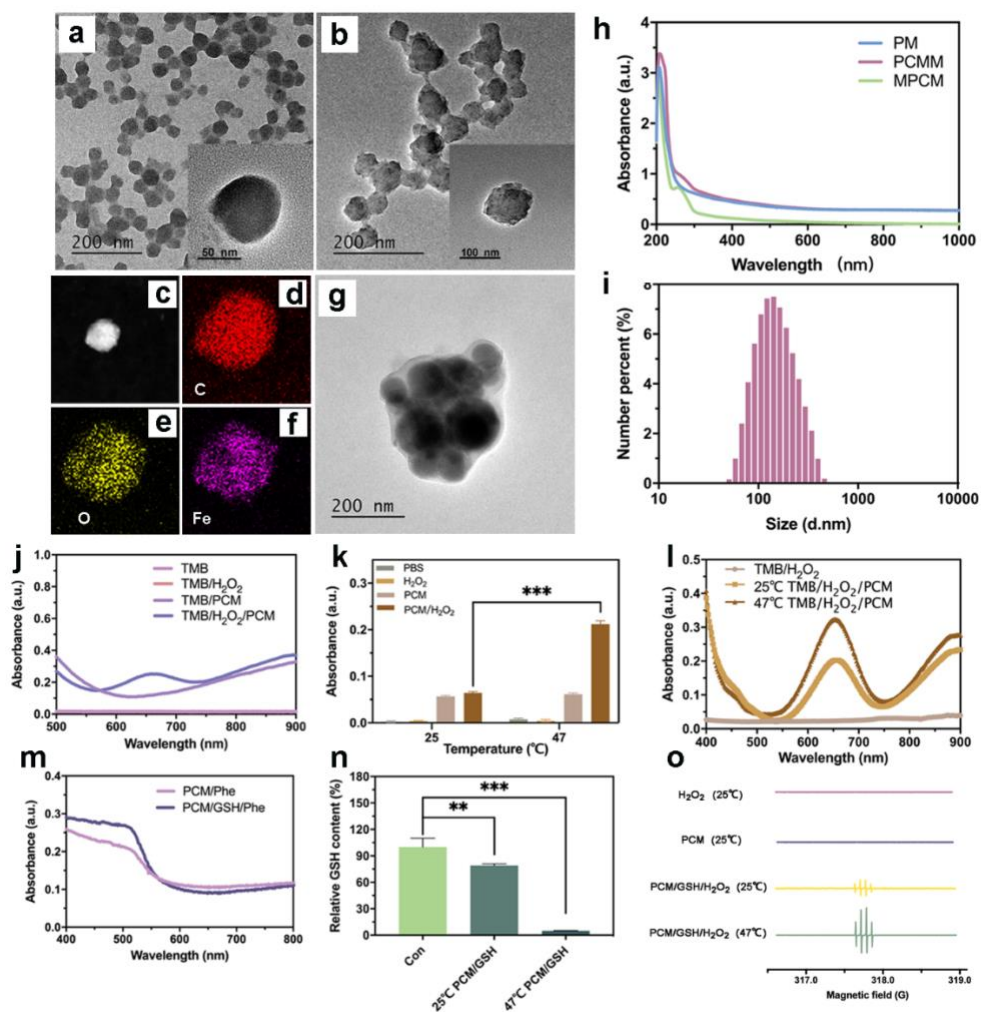
320 The preparation of PCMM includes four steps. First, PPy NPs were polymerized at
321 room temperature. The TEM image shows that PPy NPs are spherical particles with an
322 average diameter of about 40 nm (Fig. 1a). PM NPs were obtained at a high temperature
323 of 75 °C. The TEM image shows that PM NPs have a spherical structure with an
324 average diameter of about 80 nm (Fig. 1b). As shown in Fig. S1, the DLS image shows
325 that the average hydrodynamic diameters of PPy and PM are 68.1 nm and 106 nm,
326 respectively. The mapping image clearly shows the elemental distribution of PM NPs.
327 It is clear that iron is abundantly distributed in PM NPs (Fig. 1cdef). Next, the obtained
328 PM NPs were mixed with the CTD solution and stirred for 24 h to obtain the PCM NPs.
329 The absorbance of the supernatant was measured, and the loading efficiency of CTD
330 was approximately 29.02%. Finally, the cell membrane was extracted from RAW264.7
331 cells by differential centrifugation. The resulting mixture was passed through a 200 nm
332 polycarbonate membrane no less than 11 times to obtain PCMM NPs camouflaged by
333 MPCM. The TEM image clearly shows that the PCM NP is completely wrapped by the
334 phospholipid bilayer (Fig. 1g). As shown in the UV-Vis-NIR absorption spectrum (Fig.

335 1h), the characteristic peaks (260 nm) of cell membranes were also found in PCMM
336 NPs. As shown in Fig. 1i, the DLS image shows that the average hydrodynamic
337 diameter of the NPs after coating is about 200 nm. The above results indicate that PCM
338 NPs were successfully encapsulated by MPCM.

339 **3.2 Ability of PCM to generate ROS and reduce GSH**

340 To confirm that PCM NPs can produce ROS in the presence of H₂O₂, TMB was used
341 to evaluate the efficiency of peroxidase. As shown in Fig. 1j, by comparing the
342 absorption value at 650 nm, it is obvious that PCM can indeed consume H₂O₂ in the
343 presence of H₂O₂. As shown in Fig. 1k and l, by comparing the absorption values of
344 PCM/H₂O₂ (25 °C) and PCM/H₂O₂ (47 °C) at 650 nm, it can be observed that increasing
345 the reaction temperature can indeed increase this peroxidase-like activity. As an
346 important intracellular antioxidant, GSH plays an irreplaceable role in protecting cells
347 against increased intracellular oxidative stress(30). Therefore, we hypothesize that Fe³⁺
348 can be reduced to Fe²⁺ by GSH and that Fe²⁺ can form a citrinine complex with 1,10-
349 phenanthroline monohydrate (Phe). As shown in Fig. 1m, the absorption peak at 525
350 nm in the UV-Vis absorption spectrum indicate that Fe³⁺ in PCMM does have the ability
351 to consume GSH. Fig. 1n also suggests that high temperature can improve this ability.
352 To analyse the types of ROS generated, 5,5-dimethyl-1-pyrroline-N-oxide (DMPO)
353 was used as an electron paramagnetic resonance capture probe. As shown in Fig. 1o,
354 PCM and H₂O₂ alone cannot produce obvious characteristic spectra at room
355 temperature. At 47 °C, in the presence of GSH, PCM/H₂O₂ induced the generation of a

356 characteristic spectrum of $\cdot\text{OH}$ with a relative intensity of 1:2:2:1. In the case of 25 °C,
 357 the response intensity is obviously not as good as that at 47 °C. This suggests that the
 358 generation efficiency of the ROS increases at high temperature.



359
 360 **Fig. 1.** a) TEM image of PPy NPs. b) TEM image of PM and c) corresponding dark
 361 field TEM image and element mapping of d) carbon (C, red), e) oxygen (O, yellow)
 362 and f) iron (Fe, purple) in the selected area. g) TEM image of PCMM. h) UV-Vis
 363 absorption spectra of PM, MPCM and PCMM. i) Average hydrodynamic size of
 364 PCMM. j) UV-Vis absorption spectra of TMB solutions treated with different groups.
 365 k) Absorbance of TMB at 650 nm after incubation for 5 min under the specified

366 conditions. l) UV-Vis absorption spectra of TMB and H₂O₂ incubated with PCM at
367 different temperatures. m) UV-Vis absorption spectra of the PCM/Phe and
368 PCM/GSH/Phe groups. n) Evaluation of the GSH consumption capacity of PCM NPs
369 at different temperatures with the GSH Kit. o) EPR spectrum of PCM with DMPO as
370 the capture agent under specified conditions. *, P<0.05; **, P<0.01; ***, P <0.001.

371 **3.3 Photothermal performance of PCMM NPs**

372 To determine the photothermal performance of PCMM NPs, photothermal conversion
373 experiments were conducted. The suspensions of PCMM NPs with gradient
374 concentrations (25, 50 and 75 µg/mL) were exposed to an 808 nm laser, and each
375 concentration of the PCMM NPs was exposed to three light intensities (500, 750 and
376 1000 mW/cm²) for 10 min. DMEM complete medium was used as a control group. As
377 shown in Fig. 2c and S2ab, the temperature of the PCMM suspension shows a clear
378 concentration-dependent increase over time. As shown in Fig. 2d and S3ab, the
379 temperature of the PCMM suspension shows a clear light intensity-dependent increase
380 over time. In a 37 °C environment, after 1000 mW/cm² laser irradiation, the maximum
381 temperature (T_{max}) of PCMM NPs with a concentration of 75 µg/mL quickly reached
382 55.9 °C while the T_{max} of DMEM only increased to 38.8 °C under the same conditions.

383 Due to the satisfactory photothermal conversion characteristics, PCMM NPs also
384 provide high contrast in infrared thermal imaging (Fig. 2ab, S2cd and S3cd). The
385 infrared thermal imaging mode can be used to identify the location of the PTT agent
386 and provide real-time monitoring of the PTT treatment effect. The photothermal

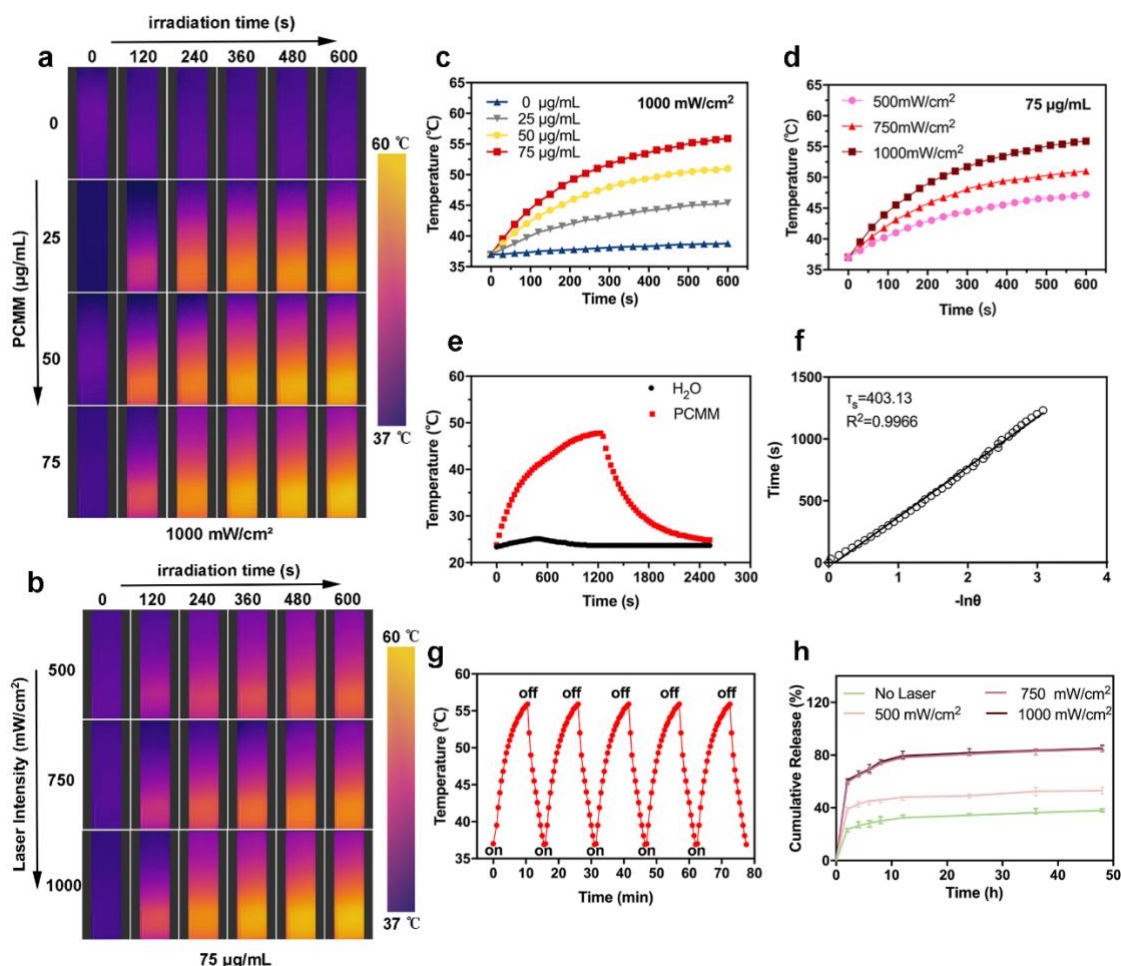
387 conversion efficiency (η) of PCMM NPs was further calculated according to the method
388 reported in the literature(31). Based on the obtained data shown in Fig. 2e, the following
389 formula was used to calculate the η of PCMM NPs:

$$390 \quad \eta = \frac{hS(T_{max} - T_{max,water})}{I(1 - 10^{-A_\lambda})}$$

391 where h represents the heat transfer coefficient, S is the area perpendicular to the cross-
392 section of the laser transmitter, T_{max} and $T_{max,water}$ are the highest temperatures that the
393 nanoparticle sample solution and pure water can respectively reach after laser
394 irradiation, I is the laser power, and A_λ is the absorption value of a sample with a UV-
395 VIS-NIR spectrum of 808 nm. The time constant (τ_s) was determined from the cooling
396 cycle curve at 403.13 s (Fig. 2f), and the η of PCMM was calculated as 39.92%.

397 Compared with some excellent photothermal agents that have been reported, PCMM
398 still performs well (32, 33). The above results suggest that PCMM has strong potential
399 for PTT application. The photostability test of the PCMM was performed. After five
400 repeated heating cycles, the PCMM can still reach the efficiency of the first heating
401 cycle under light exposure (Fig. 2g). The above results suggest that the photothermal
402 effect of PCMM is comparable to that of other classic PTT reagent (such as Au NPs).
403 Drug release curve (Fig. 2h) showed that the average release rate of CTD within 48 h
404 without NIR laser irradiation was only 38.03%, and the average release rate of CTD
405 within 48 h irradiated by 500 mW /cm² NIR laser irradiation was 53.09%, while the
406 average release rate of CTD within 48 h irradiated by 750 and 1000 mW /cm² NIR laser
407 irradiation was very similar, reaching more than 84%. We hypothesize that this may be

408 because both 750 and 1000 mW /cm² photothermal effects are sufficient to rupture the
 409 macrophage membrane and release almost all CTDs.



410

411 **Fig. 2.** Photothermal performance of PCMM in vitro. a) Near-infrared thermal images
 412 of PCMM suspension at three concentrations with 1000 mW/cm² Near-infrared laser
 413 irradiation (808 nm) for 10 min and b) Near-infrared thermal images of PCMM
 414 suspension (75 µg/mL) with three light intensities of Near-infrared laser irradiation
 415 (808 nm) for 10 min. c) The temperature (°C) of PCMM at 1000 mW/cm² Near-infrared
 416 laser irradiation (808 nm) for 10 min. d) The temperature (°C) of PCMM (75 µg/mL)
 417 with three light intensities of Near-infrared laser irradiation (808 nm) for 10 min. e)

418 Heating and cooling curves of the PCMM suspension (75 $\mu\text{g/mL}$) and deionized water
419 at room temperature. f) The plot of cooling time versus negative natural logarithm of
420 the temperature driving force. g) Temperature change of the PCMM suspension (75
421 $\mu\text{g/mL}$) under laser irradiation for 5 on/off cycles. h) Drug release of PCMM with three
422 light intensities of Near-infrared laser irradiation (808 nm) for 10 min. Unless otherwise
423 specified, the photothermal experiments were performed at 37 $^{\circ}\text{C}$.

424 **3.4 Biocompatibility**

425 Biocompatibility is essential for nanomedicine used in cancer treatment. Therefore, we
426 tested the hemolysis behaviour after incubation with red blood cells (RBCs) and the
427 result showed negligible hemolysis (Fig. S4a). In addition, standard CCK-8 analysis
428 was performed on HepG2 cells and 293T cells to evaluate the biosafety of the
429 nanoparticles. As shown in Fig. S4b and c, after 48 h of incubation with PM, PCM and
430 PCMM (25, 50 and 75 $\mu\text{g/mL}$), the cell viability was greater than 95%. The above
431 results show that PCMM has good biocompatibility and blood compatibility.

432 **3.5 Cell uptake**

433 To evaluate the targeting ability of the coated MPCM, the uptake behaviour of PDM
434 and PDMM in RAW264.7, 293T, HepG2 and HepA1-6 cells was studied by CLSM
435 and flow cytometry. As shown in Fig. 3a, the CLSM results show that the cellular
436 uptake efficiency of PDMM in HepG2 and HepA1-6 cells is significantly higher than
437 that of PDM. This indicated that PCMM had higher selectivity to HepG2 and HepA1-
438 6 cells. The cellular uptake efficiency of PDMM in RAW264.7 and 293T cells is

439 significantly lower than that of PDM. This may be due to the ability of MPCM's surface
440 biomacromolecules to recognize tumour cells and respond to signal molecules in
441 tumour regions, so that MPCM can actively recruit to tumour tissues and increase
442 retention and accumulation. Flow cytometry (Fig. S5) and its quantitative results (Fig.
443 3b) showed that PDMM had a higher degree of internalization in HepG2 and HepA1-6
444 cells. The above results indicate that PDMM has a high active targeting ability against
445 tumour cells.

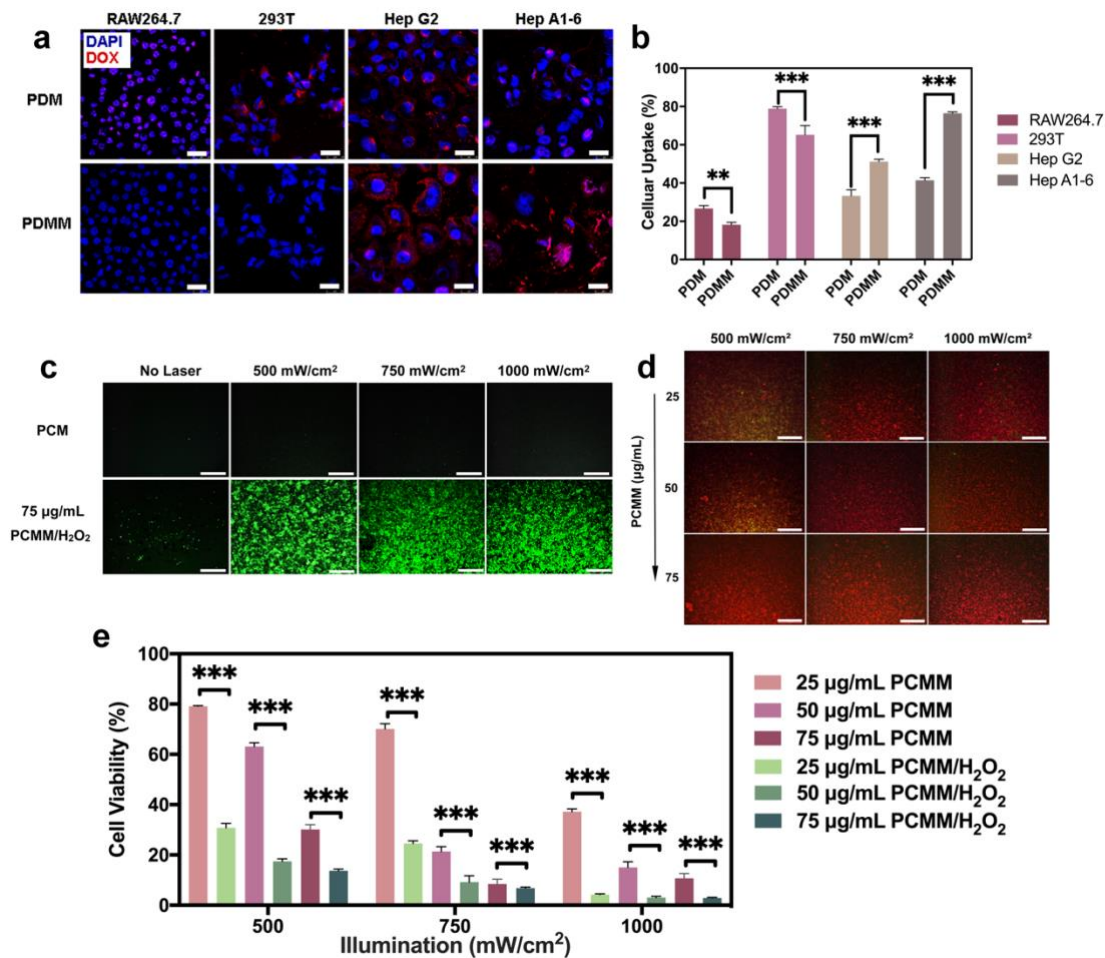
446 **3.6 Generation and determination of ROS**

447 As shown in Fig. 3c and S6, HepG2 cells treated with DMEM or PCM only generated
448 a small amount of ROS under various light intensities. PCMM exhibited a ROS
449 generation level similar to that of DMEM without NIR irradiation. In the case of
450 PCMM/H₂O₂ at 25 µg/mL, the ROS response was gradually emerging after irradiation
451 with light intensities of 500 mW/cm² and 750 mW/cm² for 10 min. After irradiation
452 with light intensity of 1000 mW/cm² at 25 µg/mL of PCMM and 750 mW/cm² at 50
453 µg/mL of PCMM for 10 min, the generation level of ROS was greatly improved. We
454 speculate that the reason for this effect might be that the temperature increases in
455 response to the photothermal agent irradiated with the laser light, causing the MPCM
456 to rupture and a large amount of iron ions to be released.

457 **3.7 Cytotoxicity of PTT and combination therapy in vitro**

458 Encouraged by the effective photothermal conversion performance, ROS generation
459 ability and tumour cell-specific targeting characteristics, the in vitro antitumour ability

460 of PCMM were further evaluated in CLSM, flow cytometry and CCK-8 analysis. We
461 tested the PTT toxicity and combination therapy toxicity respectively. The cytotoxicity
462 of PTT was obtained by formulating gradient concentrations of PCMM (25, 50 and 75
463 $\mu\text{g}/\text{mL}$) with cells and DMEM complete medium with or without H_2O_2 under different
464 light intensities (500, 750 and $1000 \text{ mW}/\text{cm}^2$) for 10 min. As shown in Fig. S7, the
465 results of flow cytometry showed that the mortality rate reached more than 80% under
466 the conditions of $50 \mu\text{g}/\text{mL}$ and $1000 \text{ mW}/\text{cm}^2$ as well as $75 \mu\text{g}/\text{mL}$ and 750 and 1000
467 mW/cm^2 . Combination therapy was obtained by irradiating cells with H_2O_2 -activated
468 PCMM (25, 50 and $75 \mu\text{g}/\text{mL}$) under different light intensities (500, 750 and 1000
469 mW/cm^2) for 10 min. As shown in Fig. 3d, the CLSM results showed that at a
470 concentration of $25 \mu\text{g}/\text{mL}$, it had a significant killing effect on most cells. As shown
471 in Fig. 3e, the CCK-8 results more directly showed the gap between PTT and
472 combination therapy, which indicated that combination therapy is a promising
473 treatment strategy.



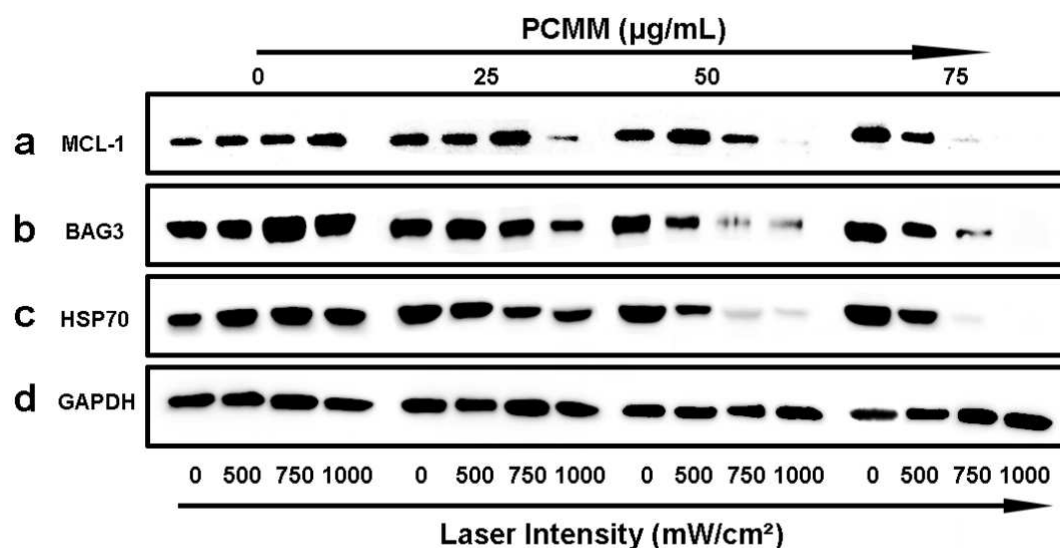
474

475 **Fig. 3.** a) Confocal laser images of RAW264.7, 293T, HepG2 and HepA1-6 treated
 476 with PDM or PDMM. Scale bar: 25 μm . b) Quantitative graphs of PDM and PDMM
 477 uptake by four types of cells. c) The ability to generate ROS in cells recorded by CLSM.
 478 Scale bar: 200 μm . d) Fluorescence images of HepG2 cells treated with different
 479 PCMM/H₂O₂ concentrations upon different light intensities for 10 min. Live cells
 480 (green); dead cells (red). Scale bar: 500 μm . e) CCK-8 was used to detect the viability
 481 of PTT and combination therapy (*, P<0.05; **, P<0.01; ***, P <0.001).

482 3.8 Exploration of the inhibitory effect of PCMM on HSR

483 In this context, we are very interested in the inhibitory effect of PCMM on HSR. In this
 484 article, we only discuss trigger conditions from PTT. We evaluated the conditions of

485 the HSR by monitoring the performance of several important HSPs that are involved.
486 HSP70 and BAG3 are two important HSPs produced by cells during HSR. MCL-1
487 belongs to Bcl-2. The family of antiapoptotic proteins prevents cells from entering the
488 apoptotic state by blocking the release of cytochrome C from mitochondria(34). As
489 shown in Fig. 4a,b and c, the 0 $\mu\text{g}/\text{mL}$ group represented the HSR of H22 tumour cells
490 when PTT was applied. It could be seen that the greater the light intensity, the more
491 severe the HSR was(18). After HepG2 cells were irradiated with 25 $\mu\text{g}/\text{mL}$ of PCMM
492 upon 750 and 1000 mW/cm^2 , the expression of HSP70, BAG3 and MCL-1 were down-
493 regulated with the increase of light intensity. After 50 and 75 $\mu\text{g}/\text{mL}$ PCMM treatments,
494 HSP70, BAG3 and MCL-1 all decreased sharply after 750 and 1000 mW/cm^2
495 irradiation. Combined with the heating curve in Fig. 2c and S2ab, we found that groups
496 with similar expression levels of HSP70, BAG3 and MCL-1 had similar treatment
497 temperature, such as 25 $\mu\text{g}/\text{mL}+1000 \text{ mW}/\text{cm}^2$ and 50 $\mu\text{g}/\text{mL}+500 \text{ mW}/\text{cm}^2$. We
498 speculate that this result may be because the MPCM ruptures due to the increase in
499 temperature, and the CTD loaded in the PCMM is released, which has an inhibitory
500 effect on the expression of HSPs. Combined with the drug loading rate, it was
501 calculated that at 14.5 $\mu\text{g}/\text{mL}$ of CTD, HSR could be largely suppressed. HSR was
502 absolutely suppressed at 21.75 $\mu\text{g}/\text{mL}$ of CTD. Overall, the idea of using PCMM to
503 improve the therapeutic effect of PTT by inhibiting HSR is very promising.



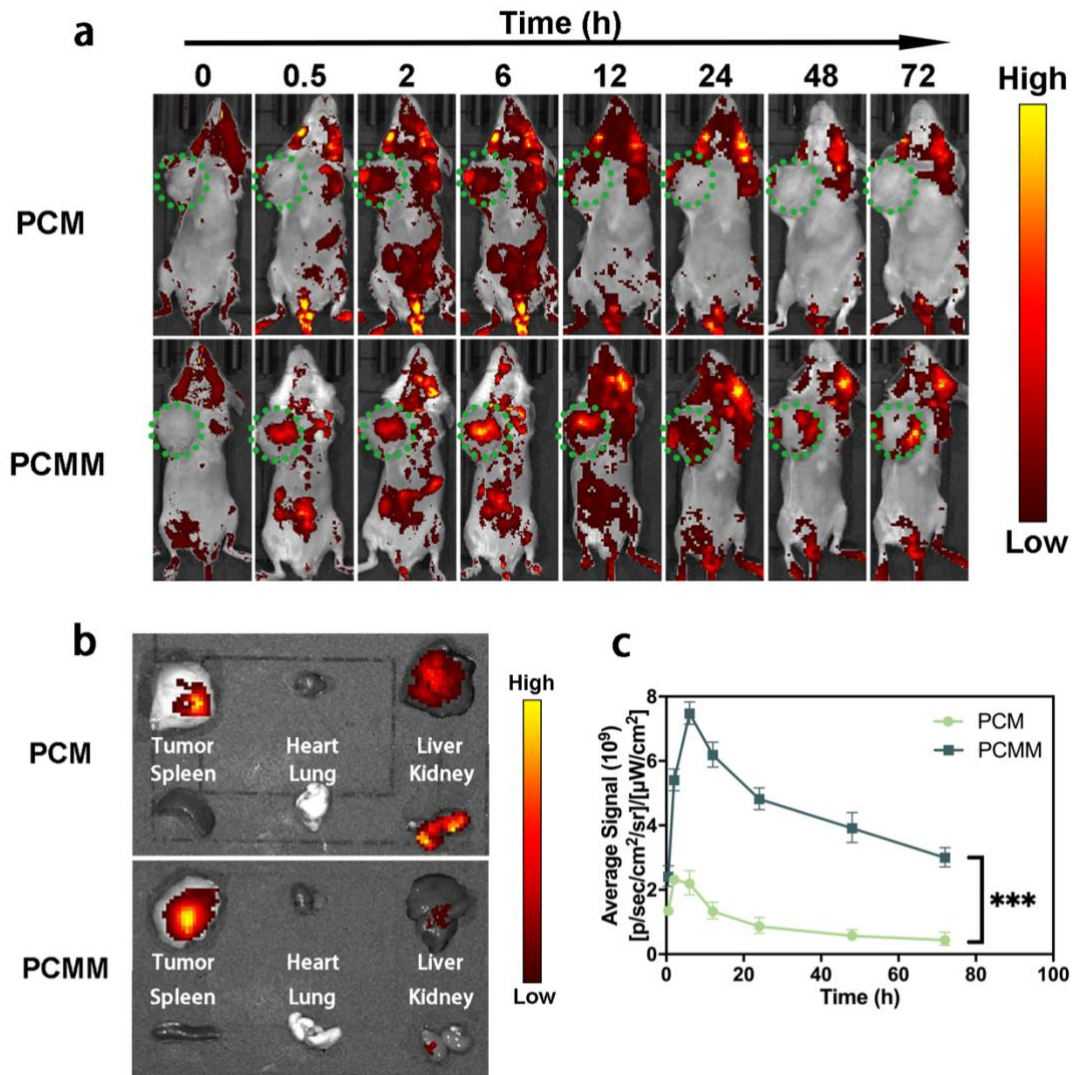
504

505 **Fig. 4.** a), b), c) and d) are the protein expression of MCL-1, BAG3, HSP70 and
 506 GAPDH after treating HepG2 cells with different concentrations of PCMM and
 507 different light intensities for 10 min.

508 **3.9 Distribution of PCMM in vivo**

509 To observe the targeting ability of PCMM more intuitively, we monitored the
 510 distribution of PCMM in vivo at different times using a live imaging instrument. As
 511 shown in Fig. 5a, compared with PCM, PCMM concentrates in the tumour more rapidly.
 512 After three days of testing, accumulation of PCMM in the tumour site can still be
 513 observed, which shows the long cycle capacity conferred by the MPCM coating. As
 514 shown in Fig. 5b, ex vivo images of tumours and organs show that mice in the PCMM
 515 group had significantly higher drug residues in tumour and lower hepatorenal
 516 accumulation compared to the PCM group. This may be because the membrane coating
 517 of macrophages reduces the absorptive capacity of the reticuloendothelial system (RES)
 518 of the liver and kidney(24, 35). Fig. 5c shows the average fluorescence intensity of the

519 tumour tissue during the entire process. 12 h after injection of PCMM, the average
 520 fluorescence intensity of the tumour tissue was the highest, and a strong fluorescence
 521 signal persisted within three days.



522

523 **Fig. 5.** a) Distribution of PCM and PCMM in vivo within 72 h; b) Ex vivo imaging of
 524 tumour and organs at 72 h; c) Average signal intensity of the tumour site within 72 h
 525 (*, $P < 0.05$; **, $P < 0.01$; ***, $P < 0.001$).

526 **3.10 Antitumour effect of PCMM in vivo**

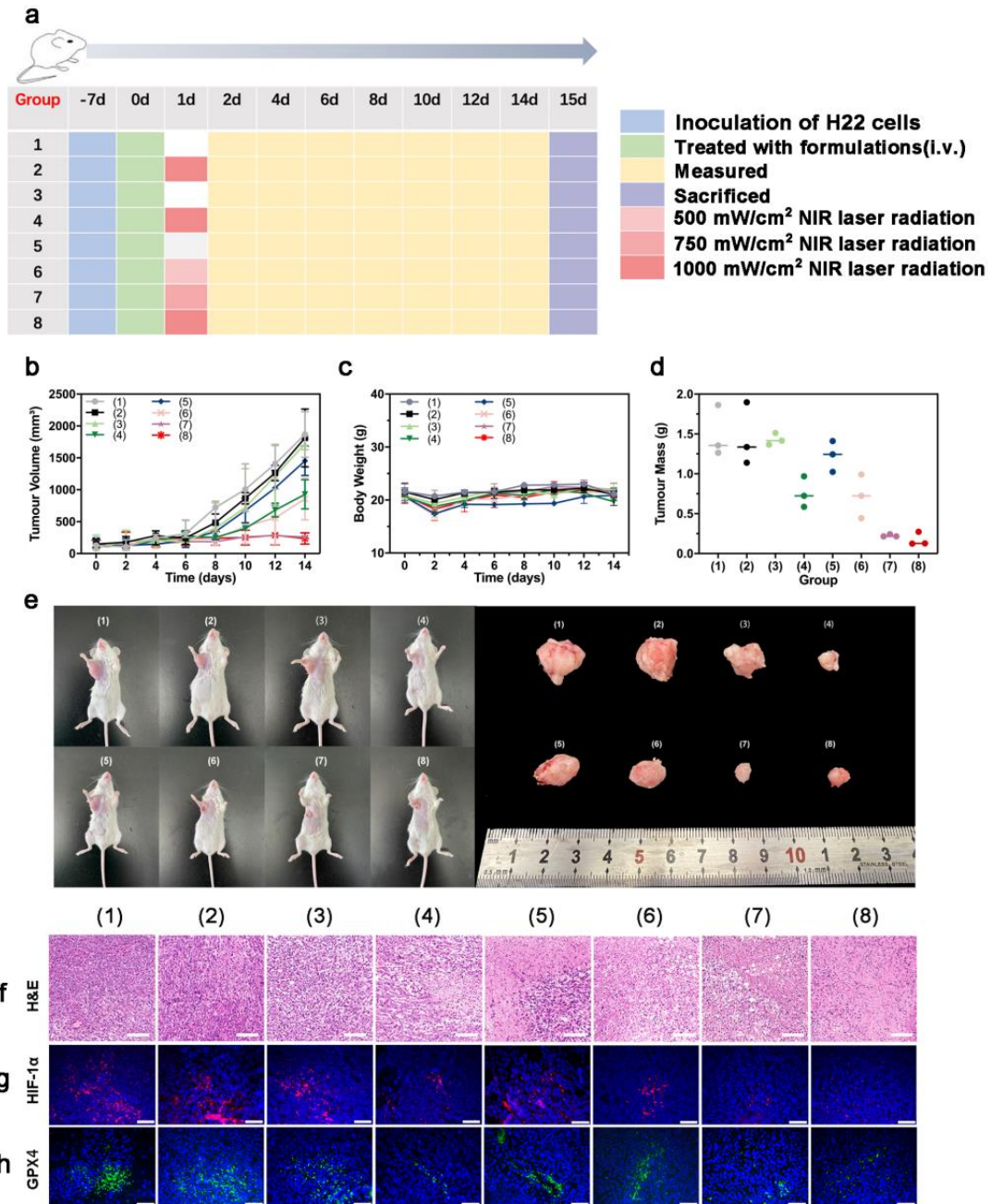
527 After investigating the conditions for inhibiting the HSR, we selected the most
528 representative treatment conditions for in vivo study. The in vivo experiment was
529 conducted according to the schedule shown in Fig. 6a. H22 cells were used to establish
530 a tumour model in the right armpit of BALB/c mice at one week in advance. On the
531 first day of treatment, PBS, PMM and PCMM (5 mg/kg, 0.1 mg/kg CTD, 100 μ L) were
532 intravenously injected into the mice. Within 12 h after administration, the tumours of
533 the mice were irradiated with an NIR laser (808 nm) for 10 min.

534 The tumour size was measured every 2 days throughout the experiment, and the tumour
535 volume was plotted over time. Fig. 6b shows the changes in tumour volume during the
536 entire experiment. Due to the absence of near-infrared radiation, tumours in the PBS,
537 PMM and PCMM groups showed a natural growth trend. After NIR irradiation, mice
538 treated with PBS showed the same growth trend as PBS alone, which means that light
539 irradiation is harmless. The mice treated with PMM+1000 mW/cm² showed a strong
540 inhibition of tumour growth in the first ten days, benefitting from the combination
541 therapy of PTT and the Fenton reaction delivered by PMM. Unfortunately, after 12
542 days of treatment, the tumours recurred and grew rapidly. During the entire treatment
543 cycle, the tumours in the PCMM+1000 mW/cm² group were effectively suppressed,
544 and no recurrence was observed during the entire experiment. Compared with mice
545 treated with PMM+1000 mW/cm², this satisfactory result may be due to laser
546 irradiation triggering the release of CTD, thereby inhibiting the HSR of the tumour and
547 enhancing the PTT effect of PCMM combined with chemotherapy and Fenton reaction.
548 Thus, the tumour is completely suppressed. Fig. 6c shows the body weight of the mice

549 during the entire treatment period, which was maintained at a stable level, indicating
550 the safety of the drug. Fig. 6d shows tumour quality after treatment. Concordant with
551 the above results, the mass of tumour was significantly reduced in PCMM plus three-
552 light intensity laser irradiation group, and the effect was similar in 750 mW/cm² and
553 1000 mW/cm². Fig. 6e shows representative pictures of the mice and tumours after
554 different treatments. It can be observed that the tumour volume in the group without
555 laser irradiation was significantly larger than that in the group with laser irradiation.
556 PCMM+750 mW/cm² and PCMM+1000 mW/cm² have similar therapeutic effects. To
557 achieve favorable PTT antitumour efficacy, the dosage of NIR light usually needed to
558 reach 1.5–4.8 W/cm², and the therapeutic platform we developed can achieve effective
559 treatment within the bio-tissue tolerance threshold values (0.33-1.0 W/cm² at 808 and
560 980 nm wavelengths)(36). Fig. 6f shows H&E staining of tumour tissue after treatment.
561 It can be seen that results similar to the above results, indicating that PCMM-mediated
562 tumour-targeted combination therapy provides a promising method for cancer
563 treatment.

564 **3.11 Immunofluorescence**

565 The tumour tissue of the treated mice was paraffin sectioned for immunofluorescence
566 experiments. As shown in Fig. 6g, the expression level of HIF-1 α in the PBS group was
567 significantly higher than that in the PCMM group treated with laser, indicating that
568 PCMM effectively improved the hypoxic internal environment. The expression of
569 GPX4 (Fig. 6h) also showed a similar trend, which suggests that iron-mediated iron
570 death also had a therapeutic effect(37, 38).



571

572 **Fig. 6.** a) Treatment schedule of H22-tumour-bearing mice treated with different
 573 formulations. b) Changes in mice tumour volume during the entire treatment period. c)
 574 Changes in body weight of the mice during the entire treatment period. d) Tumour
 575 quality after treatment e) BALB/c mice treated with different conditions and
 576 corresponding tumours. f) H&E staining of tumour tissue after treatment. Scale bar:

577 100 μm . g) Immunofluorescence image of HIF-1 α in tumour tissue (red: HIF-1 α , blue:
578 nucleus). Scale bar: 50 μm . h) Immunofluorescence image of GPX4 expression in
579 tumour tissue (green: GPX4, blue: nucleus). Scale bar: 50 μm . (1) PBS, (2) PBS+1000
580 mW/cm^2 , (3) PMM, (4) PMM+1000 mW/cm^2 , (5) PCMM, (6) PCMM+500 mW/cm^2 ,
581 (7) PCMM+750 mW/cm^2 and (8) PCMM+1000 mW/cm^2 . (*, $P < 0.05$; **, $P < 0.01$; ***,
582 $P < 0.001$).

583

584 **3.12 In vivo toxicological analysis**

585 The blood was collected from the mice for routine analysis and biochemical
586 examination, and the main organs of the mice (heart, liver, spleen, lung and kidney)
587 were collected and stained with H&E for histological analysis. As shown in Fig. S8,
588 the main blood parameters (such as RBCs, HGB and PLT) of all groups were not
589 significantly different from those of the PBS group, indicating that mice in each group
590 had no adverse symptoms, such as anaemia. The AST, UREA, and CREA data showed
591 that the liver and kidney function was normal for mice in all groups. In addition, the
592 results of histological analysis (Fig. S9) showed that the main organs of each group of
593 mice maintained normal physiological morphology, and no inflammatory response was
594 observed. In addition, except for the PCMM plus laser irradiation group, tumour
595 metastasis was observed in the liver in all groups. The above results indicated that the
596 toxicity of the nanoparticles in the body is negligible at the tested dose.

597 **4. Conclusion**

598 In short, we successfully developed a combined therapy platform (PCMM NPs) based
599 on biomimetic MOF. Under near-infrared laser irradiation, the PCMM heats up rapidly,
600 which is sufficient to trigger the rupture of the coated cell membrane and cause the
601 release of the drug, indicating that the nanoparticles have a successful thermotherapy
602 response release behaviour. The results of the cytotoxicity test showed that the death
603 rate of HepG2 cells after combined treatment was as high as 97%. The in vivo
604 experimental results showed that PCMM NPs could be delivered after intravenous
605 injection to achieve highly selective tumour targeting , with negligible adverse effects
606 on normal tissues. Both in vitro and in vivo results showed that the therapeutic efficacy
607 of PCMM+750 mW/cm² and PCMM+1000 mW/cm² was very similar, indicating that
608 the combination therapy mediated by PCMM was sufficient to effectively inhibit
609 tumour growth under the laser irradiation at the intensity within the bio-tissue tolerance
610 threshold (330-1000 mW/cm²). We explored the role of PCMM NPs in inhibiting the
611 HSR in photothermal therapy and found that 14.5 µg/ mL of CTD could effectively
612 inhibit the HSR of tumour cells. In summary, due to the versatility of its structure and
613 function, PCMM can be used as a promising nanodrug delivery system for future cancer
614 treatments.

615 ASSOCIATED CONTENT

616 **Supporting Information.**

617 The following files are available free of charge.

618 **ABBREVIATIONS**

619

620 PTT photothermal therapy; PCMM PPy-CTD@MIL-100@MPCM; HSR heat shock
621 response; MPCM macrophage cell membranes; CTD cantharidin; TME tumour
622 microenvironment.

623 **Acknowledgments**

624 Authors are grateful to their respective institutions for support.

625 **Author Contributions**

626 Xiao Cheng, Ye Liu and Zhaoming Guo conceived the project, planned the experiment,
627 and interpreted the data. Jijun Fu, Hao Zhou and Dong Wang provided technical support.
628 Junke Leng and Xiaofeng Dai performed flow cytometry for intercellular uptake
629 quantification. Kun Ma and Changhao Cui contributed to the manuscript writing and
630 editing.

631 **Funding**

632 This work is financially supported by the Dalian Science and Technology Innovation
633 Fund (2019J12GX045) and National Natural Science Foundation of China (81603049),
634 the Natural Science Foundation of Liaoning Province (2019-MS-059) and the
635 Fundamental Research Funds for the Central Universities (DUT20JC08).

636 **Availability of data and materials**

637 Not applicable.

638 **Declarations**

639 **Ethics approval and consent to participate**

640 SPF BALB/c mice were purchased from Liaoning Changsheng Biotechnology Co., Ltd.
641 (Liaoning, China). All animal procedures in this investigation were approved by the
642 Institutional Animal Care and Use Committee of Dalian University of Technology.

643 **Consent for publication**

644 No individual person's data were included in this research.

645 **Competing interests**

646 Authors declare there are no competing interests, financial and non-financial, in relation
647 to the work described.

648 **REFERENCES**

649

650

651 1. Dai Y, Xu C, Sun X, Chen X. Nanoparticle design strategies for enhanced anticancer therapy by
652 exploiting the tumour microenvironment. *Chemical Society Reviews*. 2017;46(12):3830-52.

653 2. Xiao Y, Yu D. Tumor microenvironment as a therapeutic target in cancer. *Pharmacology &*
654 *Therapeutics*. 2020:107753.

655 3. Lin H, Chen Y, Shi J. Nanoparticle-triggered in situ catalytic chemical reactions for tumour-specific
656 therapy. *Chemical Society Reviews*. 2018;47(6):1938-58.

657 4. Li W-P, Su C-H, Chang Y-C, Lin Y-J, Yeh C-S. Ultrasound-Induced Reactive Oxygen Species Mediated
658 Therapy and Imaging Using a Fenton Reaction Activable Polymersome. *ACS Nano*. 2016;10(2):2017-27.

659 5. Chen Q, Feng L, Liu J, Zhu W, Dong Z, Wu Y, et al. Intelligent Albumin-MnO₂ Nanoparticles as pH-
660 /H₂O₂-Responsive Dissociable Nanocarriers to Modulate Tumor Hypoxia for Effective Combination
661 Therapy. *Advanced Materials*. 2016;28(33):7129-36.

662 6. Fu J, Shao Y, Wang L, Zhu Y. Lysosome-controlled efficient ROS overproduction against cancer cells
663 with a high pH-responsive catalytic nanosystem. *Nanoscale*. 2015;7(16):7275-83.

664 7. Kaelin WG, Jr., Ratcliffe PJ, Semenza GL. Pathways for Oxygen Regulation and Homeostasis: The
665 2016 Albert Lasker Basic Medical Research Award. *JAMA*. 2016;316(12):1252-3.

666 8. Chen XY, Zhang HL, Zhang M, Zhao PR, Song RX, Gong T, et al. Amorphous Fe-Based Nanoagents
667 for Self-Enhanced Chemodynamic Therapy by Re-Establishing Tumor Acidosis. *Advanced Functional*
668 *Materials*. 2020;30(6):9.

669 9. Tang Z, Zhang H, Liu Y, Ni D, Zhang H, Zhang J, et al. Antiferromagnetic Pyrite as the Tumor
670 Microenvironment-Mediated Nanoplatform for Self-Enhanced Tumor Imaging and Therapy. *Adv Mater*.
671 2017;29(47).

672 10. Bokare AD, Choi W. Review of iron-free Fenton-like systems for activating H₂O₂ in advanced

- 673 oxidation processes. *J Hazard Mater.* 2014;275:121-35.
- 674 11. Chen Q, Luo Y, Du W, Liu Z, Zhang S, Yang J, et al. Clearable Theranostic Platform with a pH-
675 Independent Chemodynamic Therapy Enhancement Strategy for Synergetic Photothermal Tumor
676 Therapy. *ACS Appl Mater Interfaces.* 2019;11(20):18133-44.
- 677 12. Min H, Qi Y, Zhang Y, Han X, Cheng K, Liu Y, et al. A Graphdiyne Oxide-Based Iron Sponge with
678 Photothermally Enhanced Tumor-Specific Fenton Chemistry. *Adv Mater.* 2020;32(31):e2000038.
- 679 13. Zha Z, Deng Z, Li Y, Li C, Wang J, Wang S, et al. Biocompatible polypyrrole nanoparticles as a novel
680 organic photoacoustic contrast agent for deep tissue imaging. *Nanoscale.* 2013;5(10):4462-7.
- 681 14. Liu T, Liu W, Zhang M, Yu W, Gao F, Li C, et al. Ferrous-Supply-Regeneration Nanoengineering for
682 Cancer-Cell-Specific Ferroptosis in Combination with Imaging-Guided Photodynamic Therapy. *ACS Nano.*
683 2018;12(12):12181-92.
- 684 15. Danics L, Schvarcz CA, Viana P, Vancsik T, Krenacs T, Benyo Z, et al. Exhaustion of Protective Heat
685 Shock Response Induces Significant Tumor Damage by Apoptosis after Modulated Electro-Hyperthermia
686 Treatment of Triple Negative Breast Cancer Isografts in Mice. *Cancers.* 2020;12(9).
- 687 16. Ernst A, Hennel R, Krombach J, Kapfhammer H, Brix N, Zuchtriegel G, et al. Priming of Anti-tumor
688 Immune Mechanisms by Radiotherapy Is Augmented by Inhibition of Heat Shock Protein 90. *Frontiers*
689 *in Oncology.* 2020;10.
- 690 17. Guo ZM, Liu Y, Cheng X, Wang D, Guo SB, Jia ML, et al. Versatile biomimetic cantharidin-tellurium
691 nanoparticles enhance photothermal therapy by inhibiting the heat shock response for combined
692 tumor therapy. *Acta Biomater.* 2020;110:208-20.
- 693 18. Kim JA, Kim Y, Kwon BM, Han DC. The natural compound cantharidin induces cancer cell death
694 through inhibition of heat shock protein 70 (HSP70) and Bcl-2-associated athanogene domain 3 (BAG3)
695 expression by blocking heat shock factor 1 (HSF1) binding to promoters. *J Biol Chem.*
696 2013;288(40):28713-26.
- 697 19. Hu C, Lei T, Wang Y, Cao J, Yang X, Qin L, et al. Phagocyte-membrane-coated and laser-responsive
698 nanoparticles control primary and metastatic cancer by inducing anti-tumor immunity. *Biomaterials.*
699 2020;255:120159.
- 700 20. Li SY, Cheng H, Xie BR, Qiu WX, Zeng JY, Li CX, et al. Cancer Cell Membrane Camouflaged Cascade
701 Bioreactor for Cancer Targeted Starvation and Photodynamic Therapy. *ACS Nano.* 2017;11(7):7006-18.
- 702 21. Cao H, Dan Z, He X, Zhang Z, Yu H, Yin Q, et al. Liposomes Coated with Isolated Macrophage
703 Membrane Can Target Lung Metastasis of Breast Cancer. *ACS Nano.* 2016;10(8):7738-48.
- 704 22. Jin K, Luo Z, Zhang B, Pang Z. Biomimetic nanoparticles for inflammation targeting. *Acta Pharm Sin*
705 *B.* 2018;8(1):23-33.
- 706 23. Jin K, Luo Z, Zhang B, Pang Z. Biomimetic nanoparticles for inflammation targeting. *Acta*
707 *Pharmaceutica Sinica B.* 2018;8(1):23-33.
- 708 24. Xuan M, Shao J, Dai L, Li J, He Q. Macrophage Cell Membrane Camouflaged Au Nanoshells for in
709 Vivo Prolonged Circulation Life and Enhanced Cancer Photothermal Therapy. *ACS Appl Mater Interfaces.*
710 2016;8(15):9610-8.
- 711 25. Lee MH, Yang Z, Lim CW, Lee YH, Dongbang S, Kang C, et al. Disulfide-Cleavage-Triggered
712 Chemosensors and Their Biological Applications. *Chemical Reviews.* 2013;113(7):5071-109.
- 713 26. Kim J, Cho HR, Jeon H, Kim D, Song C, Lee N, et al. Continuous O(2)-Evolving MnFe(2)O(4)
714 Nanoparticle-Anchored Mesoporous Silica Nanoparticles for Efficient Photodynamic Therapy in Hypoxic
715 Cancer. *J Am Chem Soc.* 2017;139(32):10992-5.
- 716 27. Prasad P, Gordijo CR, Abbasi AZ, Maeda A, Ip A, Rauth AM, et al. Multifunctional Albumin-MnO₂

717 Nanoparticles Modulate Solid Tumor Microenvironment by Attenuating Hypoxia, Acidosis, Vascular
718 Endothelial Growth Factor and Enhance Radiation Response. *Acs Nano*. 2014;8(4):3202-12.

719 28. Chen X, Zhang M, Li S, Li L, Zhang L, Wang T, et al. Facile synthesis of polypyrrole@metal-organic
720 framework core-shell nanocomposites for dual-mode imaging and synergistic chemo-photothermal
721 therapy of cancer cells. *J Mater Chem B*. 2017;5(9):1772-8.

722 29. Hong JY, Yoon H, Jang J. Kinetic study of the formation of polypyrrole nanoparticles in water-soluble
723 polymer/metal cation systems: a light-scattering analysis. *Small*. 2010;6(5):679-86.

724 30. Lin L-S, Song J, Song L, Ke K, Liu Y, Zhou Z, et al. Simultaneous Fenton-like Ion Delivery and
725 Glutathione Depletion by MnO₂-Based Nanoagent to Enhance Chemodynamic Therapy. *Angewandte
726 Chemie-International Edition*. 2018;57(18):4902-6.

727 31. Roper DK, Ahn W, Hoepfner M. Microscale Heat Transfer Transduced by Surface Plasmon Resonant
728 Gold Nanoparticles. *The Journal of Physical Chemistry C*. 2007;111(9):3636-41.

729 32. Dong X, Yin W, Yu J, Dou R, Bao T, Zhang X, et al. Mesoporous Bamboo Charcoal Nanoparticles as a
730 New Near-Infrared Responsive Drug Carrier for Imaging-Guided Chemotherapy/Photothermal
731 Synergistic Therapy of Tumor. *Advanced Healthcare Materials*. 2016;5(13):1627-37.

732 33. Chen D, Wang C, Nie X, Li S, Li R, Guan M, et al. Photoacoustic Imaging Guided Near-Infrared
733 Photothermal Therapy Using Highly Water-Dispersible Single-Walled Carbon Nanohorns as Theranostic
734 Agents. *Advanced Functional Materials*. 2014;24(42):6621-8.

735 34. Yang J, Liu XS, Bhalla K, Kim CN, Ibrado AM, Cai JY, et al. Prevention of apoptosis by Bcl-2: Release
736 of cytochrome c from mitochondria blocked. *Science*. 1997;275(5303):1129-32.

737 35. Xuan M, Shao J, Dai L, He Q, Li J. Macrophage Cell Membrane Camouflaged Mesoporous Silica
738 Nanocapsules for In Vivo Cancer Therapy. *Adv Healthc Mater*. 2015;4(11):1645-52.

739 36. Lin H, Gao S, Dai C, Chen Y, Shi J. A Two-Dimensional Biodegradable Niobium Carbide (MXene) for
740 Photothermal Tumor Eradication in NIR-I and NIR-II Biowindows. *Journal of the American Chemical
741 Society*. 2017;139(45):16235-47.

742 37. Xu B, Cui Y, Wang W, Li S, Lyu C, Wang S, et al. Immunomodulation-Enhanced Nanozyme-Based
743 Tumor Catalytic Therapy. *Adv Mater*. 2020;32(33):e2003563.

744 38. Liu T, Liu W, Zhang M, Yu W, Gao F, Li C, et al. Ferrous-Supply-Regeneration Nanoengineering for
745 Cancer-Cell-Specific Ferroptosis in Combination with Imaging-Guided Photodynamic Therapy. *Acs Nano*.
746 2018;12(12):12181-92.

747

Figures

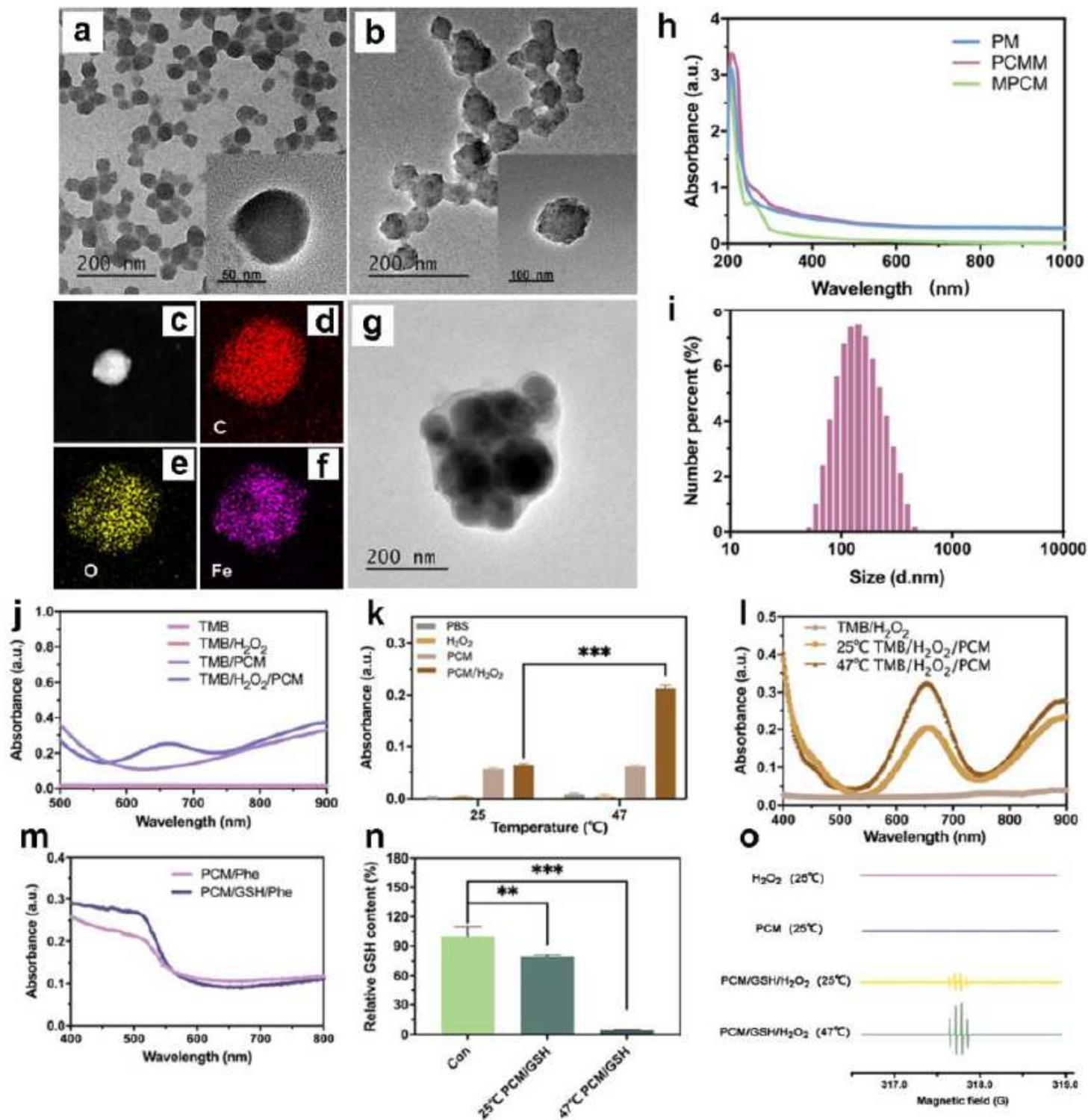


Figure 1

a) TEM image of PPy NPs. b) TEM image of PM and c) corresponding dark field TEM image and element mapping of d) carbon (C, red), e) oxygen (O, yellow) and f) iron (Fe, purple) in the selected area. g) TEM image of PCMM. h) UV-Vis absorption spectra of PM, MPCM and PCMM. i) Average hydrodynamic size

of PCMM. j) UV-Vis absorption spectra of TMB solutions treated with different groups. k) Absorbance of TMB at 650 nm after incubation for 5 min under the specified conditions. l) UV-Vis absorption spectra of TMB and H₂O₂ incubated with PCM at different temperatures. m) UV-Vis absorption spectra of the PCM/Phe and PCM/GSH/Phe groups. n) Evaluation of the GSH consumption capacity of PCM NPs at different temperatures with the GSH Kit. o) EPR spectrum of PCM with DMPO as the capture agent under specified conditions. *, P<0.05; **, P<0.01; ***, P <0.001.

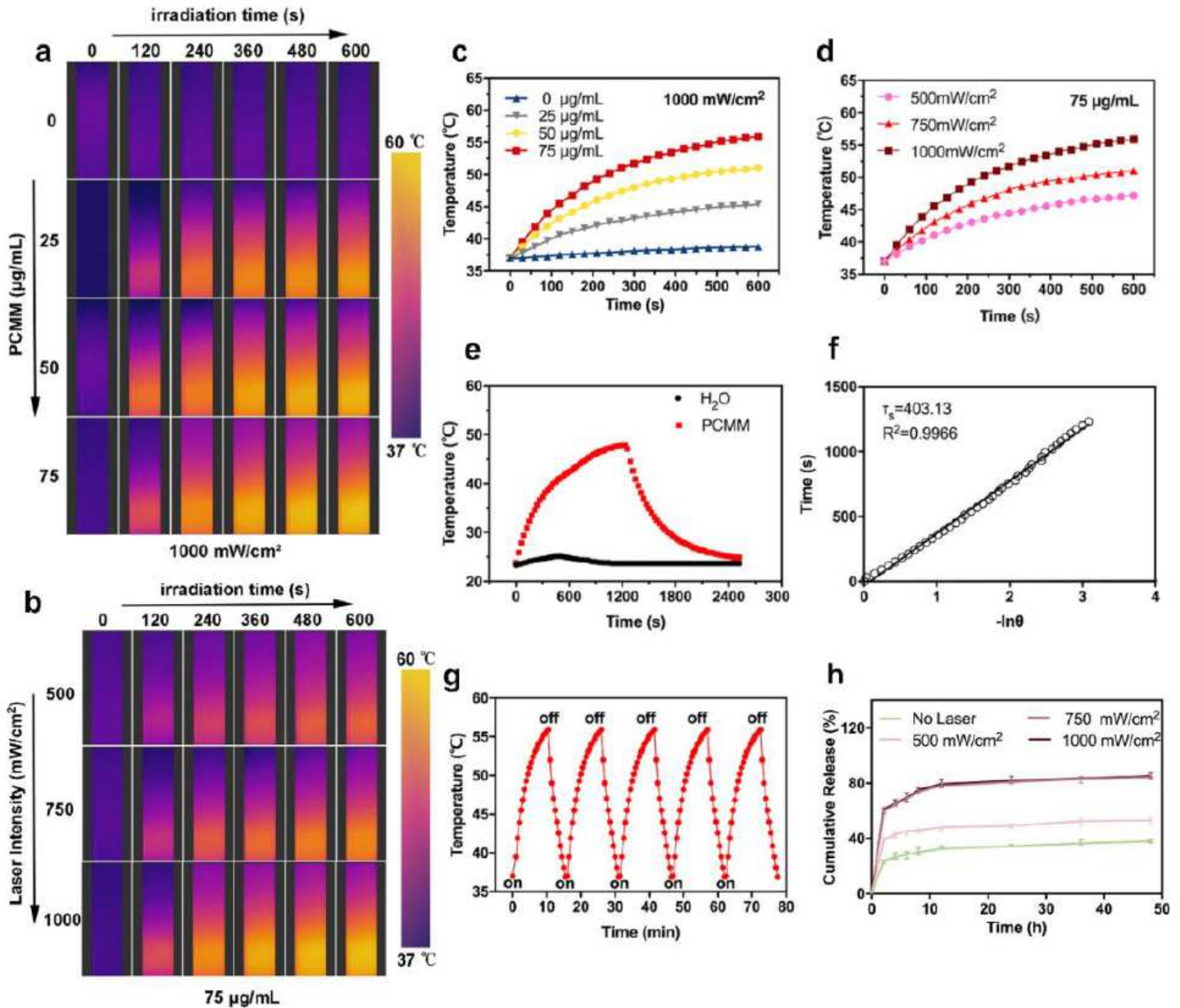


Figure 2

Photothermal performance of PCMM in vitro. a) Near-infrared thermal images of PCMM suspension at three concentrations with 1000 mW/cm² Near-infrared laser irradiation (808 nm) for 10 min and b) Near-infrared thermal images of PCMM suspension (75 µg/mL) with three light intensities of Near-infrared laser irradiation (808 nm) for 10 min. c) The temperature (°C) of PCMM at 1000 mW/cm² Near-infrared

laser irradiation (808 nm) for 10 min. d) The temperature (\boxtimes) of PCMM (75 $\mu\text{g}/\text{mL}$) with three light intensities of Near-infrared laser irradiation (808 nm) for 10 min. e) Heating and cooling curves of the PCMM suspension (75 $\mu\text{g}/\text{mL}$) and deionized water at room temperature. f) The plot of cooling time versus negative natural logarithm of the temperature driving force. g) Temperature change of the PCMM suspension (75 $\mu\text{g}/\text{mL}$) under laser irradiation for 5 on/off cycles. h) Drug release of PCMM with three light intensities of Near-infrared laser irradiation (808 nm) for 10 min. Unless otherwise specified, the photothermal experiments were performed at 37 $^{\circ}\text{C}$.

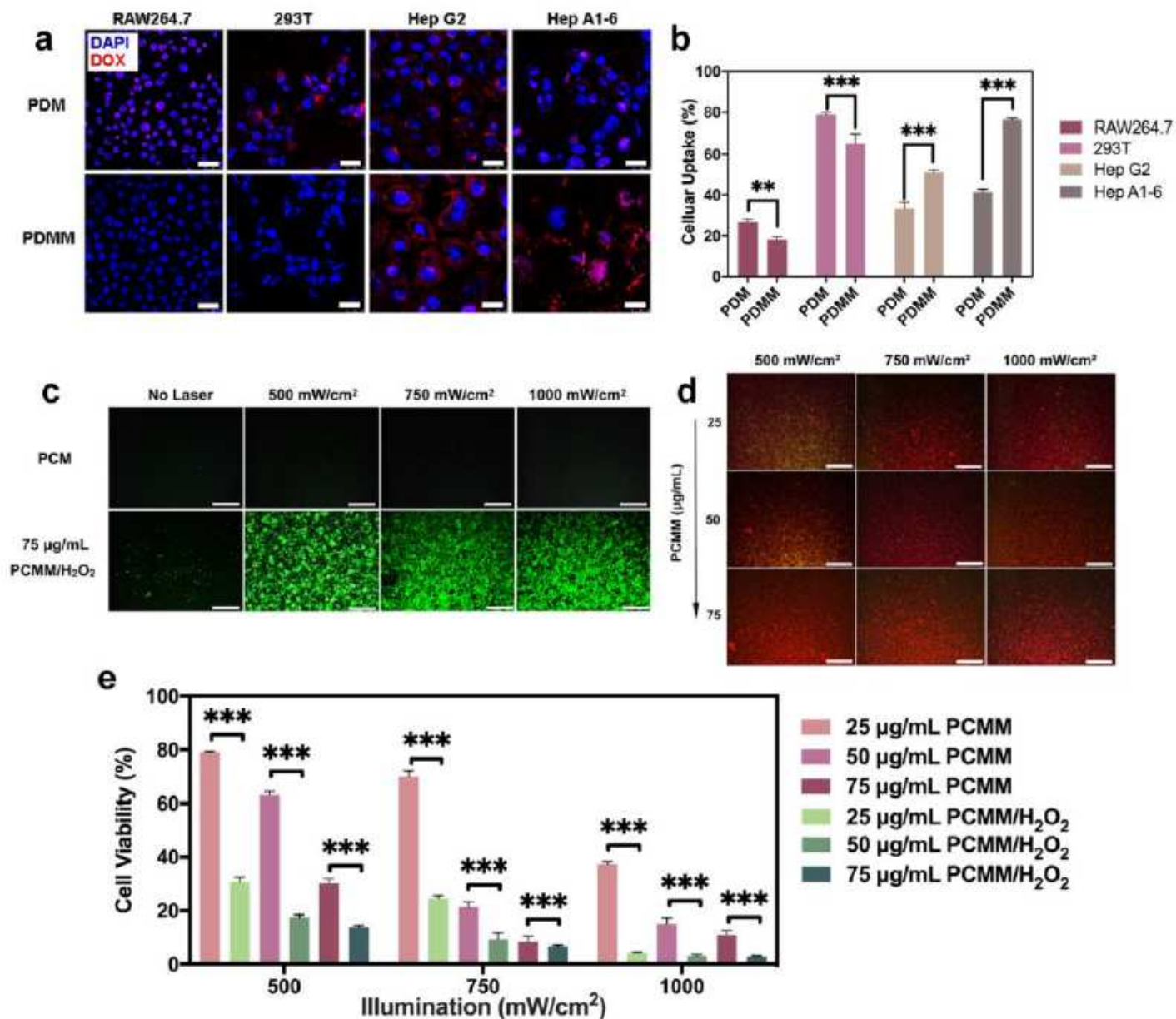


Figure 3

a) Confocal laser images of RAW264.7, 293T, HepG2 and HepA1-6 treated with PDM or PDMM. Scale bar: 25 μm . b) Quantitative graphs of PDM and PDMM uptake by four types of cells. c) The ability to generate ROS in cells recorded by CLSM. Scale bar: 200 μm . d) Fluorescence images of HepG2 cells treated with different PCMM/H₂O₂ concentrations upon different light intensities for 10 min. Live cells (green); dead

cells (red). Scale bar: 500 μm . e) CCK-8 was used to detect the viability of PTT and combination therapy (*, $P < 0.05$; **, $P < 0.01$; ***, $P < 0.001$).

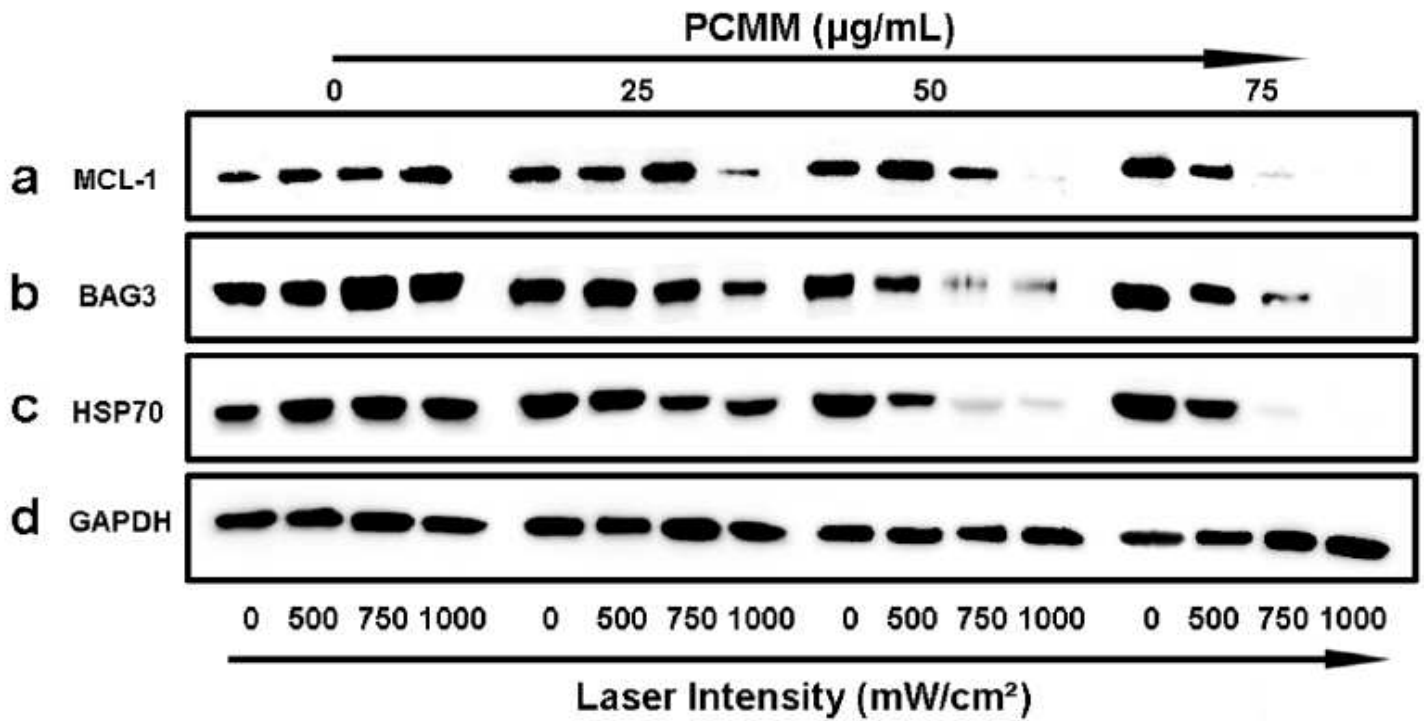


Figure 4

a), b), c) and d) are the protein expression of MCL-1, BAG3, HSP70 and GAPDH after treating HepG2 cells with different concentrations of PCMM and different light intensities for 10 min.

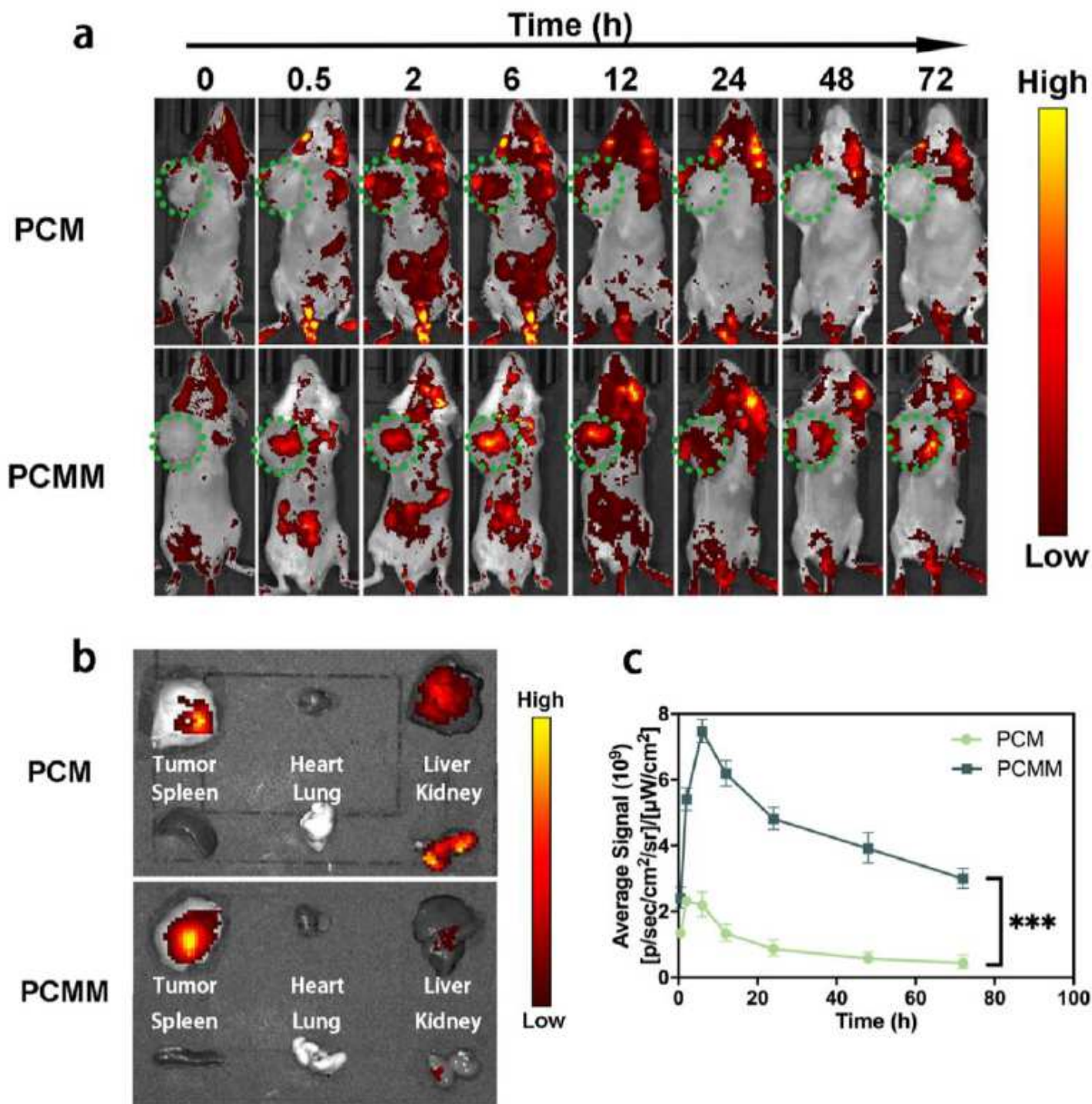


Figure 5

a) Distribution of PCM and PCMM in vivo within 72 h; b) Ex vivo imaging of tumour and organs at 72 h; c) Average signal intensity of the tumour site within 72 h (*, $P < 0.05$; **, $P < 0.01$; ***, $P < 0.001$).

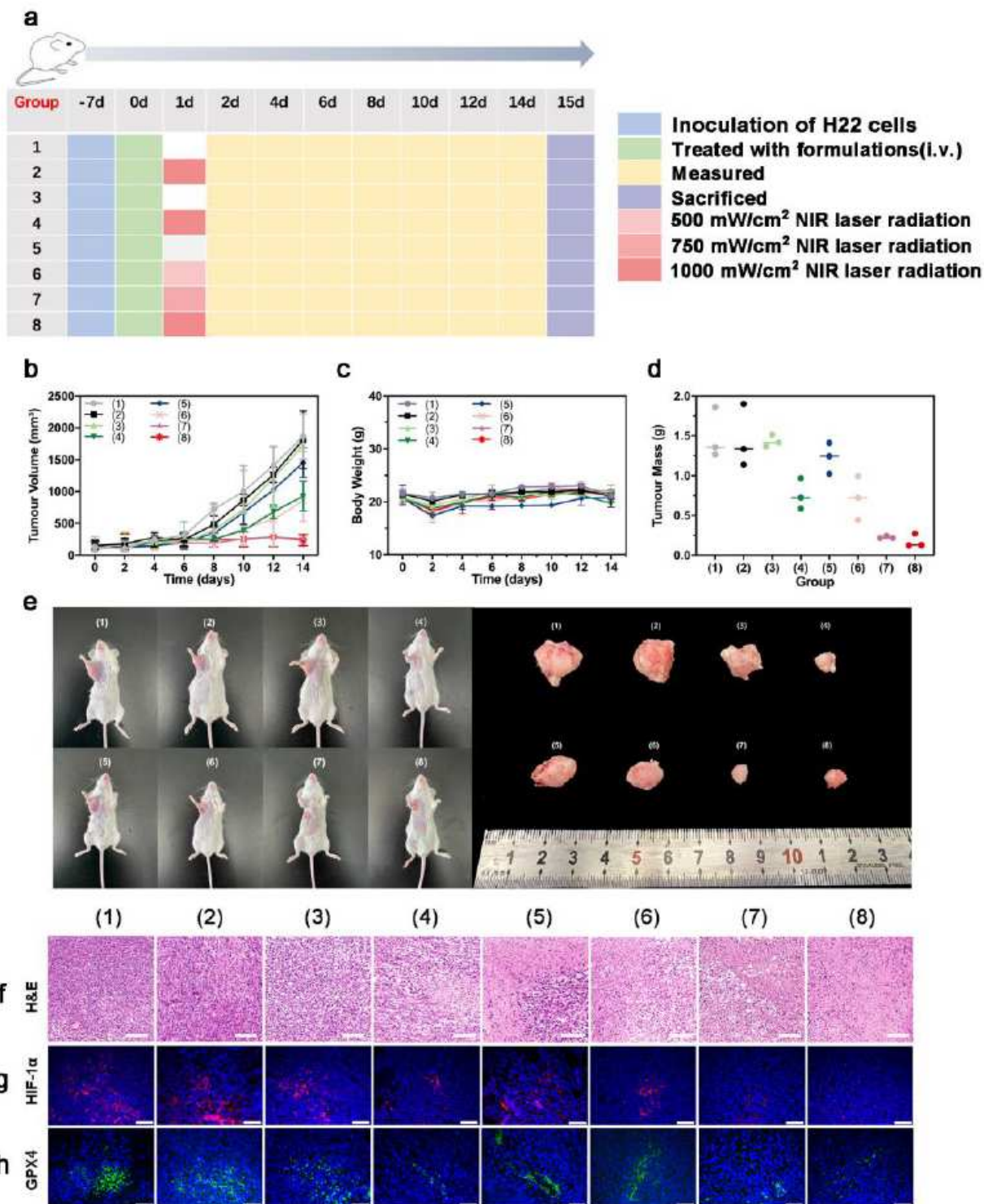


Figure 6

a) Treatment schedule of H22-tumour-bearing mice treated with different formulations. b) Changes in mice tumour volume during the entire treatment period. c) Changes in body weight of the mice during the entire treatment period. d) Tumour quality after treatment e) BALB/c mice treated with different conditions and corresponding tumours. f) H&E staining of tumour tissue after treatment. Scale bar: 100 μm . g) Immunofluorescence image of HIF-1 α in tumour tissue (red: HIF-1 α , blue: nucleus). Scale bar: 50

μm . h) Immunofluorescence image of GPX4 expression in tumour tissue (green: GPX4, blue: nucleus). Scale bar: 50 μm . (1) PBS, (2) PBS+1000 mW/cm², (3) PMM, (4) PMM+1000 mW/cm², (5) PCMM, (6) PCMM+500 mW/cm², (7) PCMM+750 mW/cm² and (8) PCMM+1000 mW/cm². (*, P<0.05; **, P<0.01; ***, P <0.001).

Supplementary Files

This is a list of supplementary files associated with this preprint. Click to download.

- [Scheme1.png](#)
- [Supplementarymaterials.pdf](#)